Epitaxial ferroelectric all-oxide varactors for application in reconfigurable RF front ends

TECHNISCHE UNIVERSITÄT DARMSTADT

vom Fachbereich
Material- und Geowissenschaften

genehmigte

Dissertation

zur Erlangung des akademischen Grades
eines Doktors der Ingenieurwissenschaften (Dr.-Ing.)

von

M.Sc. Arzhang Mani
geb. in Teheran, Iran

Darmstadt 2017
D17

Referent: Prof. Dr. Lambert Alff

Zweitreferent: Prof. Dr. Rolf Jakoby

Tag der Einreichung: 20.02.2017
Tag der Disputation: 16.06.2017

Acknowledgement

I would like to thank Prof. Dr. Lambert Alff for his constant support and insightful guidance throughout my research work at the ATFT group. Undoubtedly, concluding this work would not have been possible without his enthusiastic supervision. I am very thankful to Dr. Philipp Komissinskiy for his patience and faith in supervising me. He has continuously been a great source of scientific rigor and personal support during my entire stay at ATFT group.

I am very grateful to Prof. Dr. Rolf Jakoby for accepting to be the co-referee of this thesis and also for 3 years of enormous support for realization and harvest of the goals of this project.

I would like to convey my deepest gratitude to Prof. Dr. Wolfgang Ensinger and Prof. Dr. Wolfgang Donner for examining this work. I look forward to their constructive questions, comments, and feedback during my Ph.D. defense session.

I would like to thank all the ATFT group members for having always been supportive, informative, and friendly. In particular, I would like to thank Aldin Radetinac, Vikas Shabadi, Patrick Salg, and Dr. Mehran Vafaee Khanjani for their kind support, guidance, and companionship.

I am very much thankful to all the IMP group members at the Electrical Engineering faculty of TU Darmstadt, especially to Mohammad Nikfalazar for his patience and insightful input. Moreover, I am very grateful for the support of Dr. Yuliang Zheng, Alex Wiens and Dr. Holger Maune throughout this research work.

I would like to show my gratitude to Jürgen Schreeck and Gabi Haindl for their continuous technical support, providing me with informative advice and guidance.

Last but not the least, I would like to thank my family; my parents, brother and sister-in-law for supporting me spiritually throughout my academic track and my life in general.

Eidesstattliche Erklärung

Hiermit versichere ich an Eides statt, dass ich die vorliegende Dissertation selbstständig und nur mit den angegebenen Hilfsmitteln angefertigt habe.

Darmstadt, im Februar 2017

Arzhang Mani

Curriculum Vitae

Arzhang Mani, born on September 9th, 1985, in Tehran, Iran.

Education

Nov 2012 – Jun 2016	**Technical University of Darmstadt** Ph.D. candidate in the department of Materials Science Thesis: Epitaxial ferroelectric all-oxide varactors for application in reconfigurable RF front ends
Feb 2009 – Sep2012	**ETH Zürich, Switzerland** M.Sc. Materials Science and Economics Thesis: Resistive switching MEMS devices
Oct 2003 – Jun 2008	**Sharif University of Technology, Tehran, Iran** B.Sc. Materials Science and Engineering Thesis: Mechanical Properties & Strain Homogeneity of Copper Sheets under CGP mechanical deformation

Abstract

Modern wireless communication systems require low-cost, compact, and highly integrated tunable components such as filters, phase shifters, frequency-agile antennas, and adaptive impedance matching networks. One basic element of these components is the tunable capacitor (varactor). Among other technologies, ferroelectric thin-film varactors exhibit high power handling, low tuning voltage, quick response, high capacitance density, and good adaptability into the microwave frequency range (DC to 20 GHz). In particular, BST-based thin-film varactors have an excellent potential to reduce size, weight, cost, and to improve the functionality of wireless communication systems. Electric losses of thin-film ferroelectric varactors depend highly on the loss of the dielectric layer. In general, the choice of the bottom electrode material has a big influence on the dielectric properties and the total losses. For this reason, efforts were made to use conducting oxide materials as bottom electrodes, enabling the deposition of a dielectric layer with low defect density and misfit strain. However, due to the high electrical resistivity of the so far used electrode materials, it was concluded that oxide electrodes are too resistive for integration into microwave varactors.

In this work, the $SrMoO_3$ as a highly conducting perovskite material was integrated for the first time as the bottom electrode into thin-film BST-based varactors. Epitaxial $SrTiO_3/SrMoO_3/SrTiO_3/Ba_{0.4}Sr_{0.6}TiO_3$ heterostructure was grown onto (110) $GdScO_3$ substrate using Pulsed Laser Deposition (PLD). The microstructure of the deposited layers was characterized by X-ray diffraction techniques and Scanning Transmission Electron Microscopy (STEM). It was shown that epitaxial growth of the $SrTiO_3/SrMoO_3/SrTiO_3/Ba_{0.4}Sr_{0.6}TiO_3$ stack, locked commensurately to the $GdScO_3$ substrate, is possible. Moreover, optimization of the deposition conditions resulted in homogeneous, single-phase growth of all the layers with low mosaicity and excellent crystal quality. Using lift-off lithography, Pt/Au top electrodes were deposited by Magnetron Sputtering to enable the electrical characterization of the MIM-structured varactors. It was shown that a tunability of 50% is achievable by applying small biasing voltage of 8V. Furthermore, a quality factor of 180 at 30 MHz suggests a very low dielectric loss at the $Ba_{0.4}Sr_{0.6}TiO_3$. A commutation Quality Factor (CQF) of 10^4 at 100 MHz shows the potential of $SrMoO_3$ for integration into devices for microwave applications. As an initial step towards industrialization of this technology, a selective etching procedure for processing and fabrication of $SrMoO_3$-based electronic devices was established.

Table of Contents

1. Introduction

By the end of the 1980s, conventional processing methods for fabrication of electroceramic materials were challenged by the advent of thin film deposition techniques, such as magnetron sputtering, pulsed laser deposition (PLD), and Molecular beam epitaxy (MBE). The advantage of these processes has been to fabricate the desired material at lower temperatures with much higher control over properties[1]. The ever-increasing interest in thin film deposition techniques was accelerated by the advent of thin film High-Temperature Superconductors (HTSC) and most importantly by the progress of ferroelectric materials and Silicon and semiconductor technologies[1]. Since the 1990s, ferroelectric thin films have been receiving significant attention for integration into electronic applications. This interest stems back in the profound amount of research conducted on the ferroelectric non-volatile memories, also known as ferroelectric random access memories (FeRAMs). Moreover, Ferroelectric thin films were used in their paraelectric phase as high-permittivity dielectrics for fabrication of dynamic random access memories (DRAMs)[2].

Among other materials, the oxide thin films are anticipated to have a broad impact on the future of microelectronics, sensor systems, and RF/Microwave applications[3]. This is chiefly due to the customizable physical properties of oxide heterostructures by means of design and fabrication of novel oxide materials, and implementation of hetero- and superstructures. Furthermore, studying the oxide interfaces has become an enabling tool for understanding the electron correlations and harvesting phenomenal interfacial properties of oxide materials[4]. It is shown that mechanical strain, stoichiometry, and interfacial layers affect the properties of oxide thin films[5]. By choosing the proper substrate and growth conditions, heteroepitaxial growth of oxide layers is possible[6], [7]. Due to lattice mismatch, a mechanical strain remains at the heteroepitaxial oxide layers which could be employed to tailor the physical properties of the oxide layers[8]. It is shown that the dielectric properties of ferroelectric $Ba_xSr_{1-x}TiO_3$ thin film depend on the density and nature of the crystal defects in the crystal structure[9]. Despite the significant amount of research done on this topic, the microwave losses remain much higher than in the single crystals[10]. Previously, efforts were made to use oxide electrodes which would enable epitaxial growth of the dielectric $Ba_{1-x}Sr_xTiO_3$ (BST), with the goal of lowering the crystal defect density and thus the dielectric loss. However, it was concluded that the oxide electrodes are too resistive for microwave applications[11].

One of the most promising applications of oxide thin films is the tunable capacitors, also known as ferroelectric varactors[3]. In general, tunable microwave devices have a broad

range of applications including phase shifters, antennas, filters, voltage controlled oscillators, matching networks, electronically steerable systems, and tunable power splitters[11]–[14]. In general, telecommunication systems have observed a rapid advancement over the past years, yet there is enormous potential to unleash by enabling the fabrication of smaller devices with lower production cost, lower power consumption, and superior performance[12], [15]–[17]. Among other technologies, ferroelectric varactors offer strong electric-field-dependent dielectric permittivity which is desirable in the realization of highly tunable devices. Furthermore, most of the ferroelectric materials possess relatively low dielectric losses and high permittivity at microwave frequencies[11]. Varactors based on bulk ferroelectric materials offer low losses at microwave frequencies. However, very high tuning voltages in the range of kV are required which is a significant barrier for integration of this technology into microwave applications [3]. On the one hand, thick film ferroelectric varactors are inexpensive to fabricate. However, they have high losses and low tunability. Furthermore, the required voltage for creating the necessary electric field for tunning the thick film varactors is much higher than that of the thin film varactors [18].

In general, ferroelectric thin film technology offers the potential of miniaturization of microwave components, low losses, low power consumption, high tunability, low tuning voltages, and easy integration into planar RF circuitry [12], [13].

One of the main challenges for optimization of thin-film dielectric varactors is to lower the total loss of the varactor. A number of factors can result in electric loss of varactors, most importantly the loss of the dielectric layer and the electrode losses. Electrode losses are directly associated with the electric resistivity of the electrode material as well as the geometry of the device. By use of metallic electrodes it is possible to lower the electrode losses[19], [20]. However, the underlying bottom electrode´s crystal structure has a direct impact on the crystal structure and quality of the overlying dielectric material, and thus on the loss of the dielectric layer. In this context, previous efforts were made to use oxide electrodes as conductor layers in thin film ferroelectric varactors in order to achieve enhanced BST microstructure[21]–[23]. However, it was concluded that the oxide conductors are too resistive for integration into thin film varactors [11].

In this study, highly conducting $SrMoO_3$ has been used for the first time as the conducting bottom electrode in thin-film ferroelectric varactors based on $Ba_xSr_{1-x}TiO_3$. A number of microstructural analysis techniques have been employed to optimize the crystal structure of the conductor and dielectric layers in the varactors heterostructure. Finally, the electrical performance of SMO-based varactors has been analyzed and prospective integration into

microwave devices has been evaluated. In the following sections, the fundamental aspects of the thin film ferroelectric varactors are explained.

1.1. Dielectric materials

Dielectric materials are poor conductors of electricity. In other words, when an electric field is applied to a dielectric material, almost no electric current flows through it. This is due to the absence of loosely bonded ions or free electrons as charged carriers. Thus, in the presence of an external field, the negative ions or electrons drift in one direction, and the positive charges move in the opposite direction, also known as *polarization*. This displacement results in an internal electric field, counteracting the force of the external field and reducing the total field within the dielectric material. There are mainly four mechanisms of polarization in ceramics. Each of these mechanisms involves a short-range drift of the charged elements of the material. These mechanisms are electronic polarization, ionic (atomic) polarization, interfacial polarization, and dipolar (orientational) polarization. Among all, the dipolar polarization is the most dominant type of polarization in ferroelectric materials, resulting in dielectric constant values of 10^4 or more [24].

A perfect dielectric material is a material with no electric conductivity, harvesting and storing all the electrical energy available in the applied external electric field. In order to classify materials in terms of their dielectric response, two terms are of great significance: the *electric susceptibility* and the *electric permittivity*.

The *electric susceptibility* χ of a dielectric material is a measure of how easily a material in an external electric field is polarized. The *electric permittivity* ε represents the resistance of a material against formation of an electric field inside it. Thus, a material with higher permittivity provides higher resistance to an electric field and thus lower electric flux across it. In order to quantify the electric permittivity of various materials, the permittivity of vacuum is taken as reference. The vacuum permittivity ε_0 (also known as the permittivity of free space) is calculated to be 8.85 E-12 F/m. Thus the relative permittivity of each material to that of vacuum can be calculated using 1.1, 1.2, and 1.3.

$$K = \varepsilon_r = \varepsilon / \varepsilon_0 \tag{1.1}$$

$$K = 1 + \chi \tag{1.2}$$

$$\varepsilon = \varepsilon_0 . \varepsilon_r = (1 + \chi). \varepsilon_0 \tag{1.3}$$

where K is the dielectric constant, ε_r is the *relative electric permittivity*, D is the electric displacement field, and E is the external electric field.

Dielectric materials can have different polarization behavior in an external electric field. The dependency of the polarization and the external field defines whether the material is ferroelectric or paraelectric.

Paraelectric materials show a nonlinear polarization in an external electric field. In contrast to most of the dielectric materials, the polarization curve of the paraelectric materials is not constant with respect to the external electric field. Thus, the electrical permittivity, which is the slope of the polarization curve versus electrical field, is a function of the external electrical field. If the polarization response of a dielectric material in an external electric field is non-linear, the material is referred to as a paraelectric material. If a paraelectric material also shows a spontaneous non-zero polarization, it is known as a ferroelectric material. In ferroelectric materials, when the external field is removed, a spontaneous remnant polarization will be present. Such a polarization can be reversed by an electric field in the opposite direction, provided that the electric field is large enough. Thus, the polarization is dependent on the history of the applied electric field as well as the actual external electric field. A ferroelectric material usually becomes a paraelectric material beyond a critical temperature, called the *Curie temperature* T_c. The remnant polarization of ferroelectric materials below the Curie temperature has made them a successful candidate for fabrication of FeRAMs[25]. Furthermore, ferroelectric capacitors are used for fabrication of Radio Frequency Identification Systems (RFID) [26]. Above the *Curie temperature*, ferroelectric materials show paraelectric behavior. The paraelectric phase of the ferroelectric materials is the main physical property that thin film ferroelectric varactors rely on [11], [15]. In the following section, fundamentals of thin-film ferroelectric varactors will be presented.

1.2. Thin-film ferroelectric varactors

Thin film Ferroelectric materials have been utilized and integrated into semiconductor microelectronics and Integrated circuits (ICs) [12]. Tunable capacitors, also known as varactors, are an important element in many devices functioning in the RF and microwave frequencies. This includes phase shifters, tunable filters and voltage-controlled oscillators [27]–[30]. For commercialization and scalability of varactor technologies, utilizing the BST thin films, the following set of criteria must be met [11]:

- Low loss tangent (high quality factor) at the operation frequencies
- High tunability
- Low production cost
- Reproducibility
- Reliability

There are few other competing technologies available for the realization of tunable capacitors. The most promising varactor technologies and their advantages and disadvantages are listed in Fig. 1.1. In general, it is the application conditions which set the choice of the required technology for fabrication of tunable varactors. Among other technologies, semiconductor varactor diodes, RF MEMS varactors, and ferroelectric thin film varactors are the major candidates for the realization of varactor applications. Micro Electro Mechanical Varactors (MEMS varactors) are considered as a promising technology for the implementation of tunable varactors. MEMS varactors offer a very high quality factor. However, due to their mechanical nature, their response time is much slower than that of the ferroelectric varactors. Moreover, MEMS varactors are vulnerable to environmental conditions such as temperature shock, vibrations, and humidity [3]. The semiconductor GaAs varactors offer high tunability and reliability. However, not only are they expensive, but also their quality factor drops linearly with an increase in frequency, making this technology inept for application in frequencies higher than 20 GHz [31].

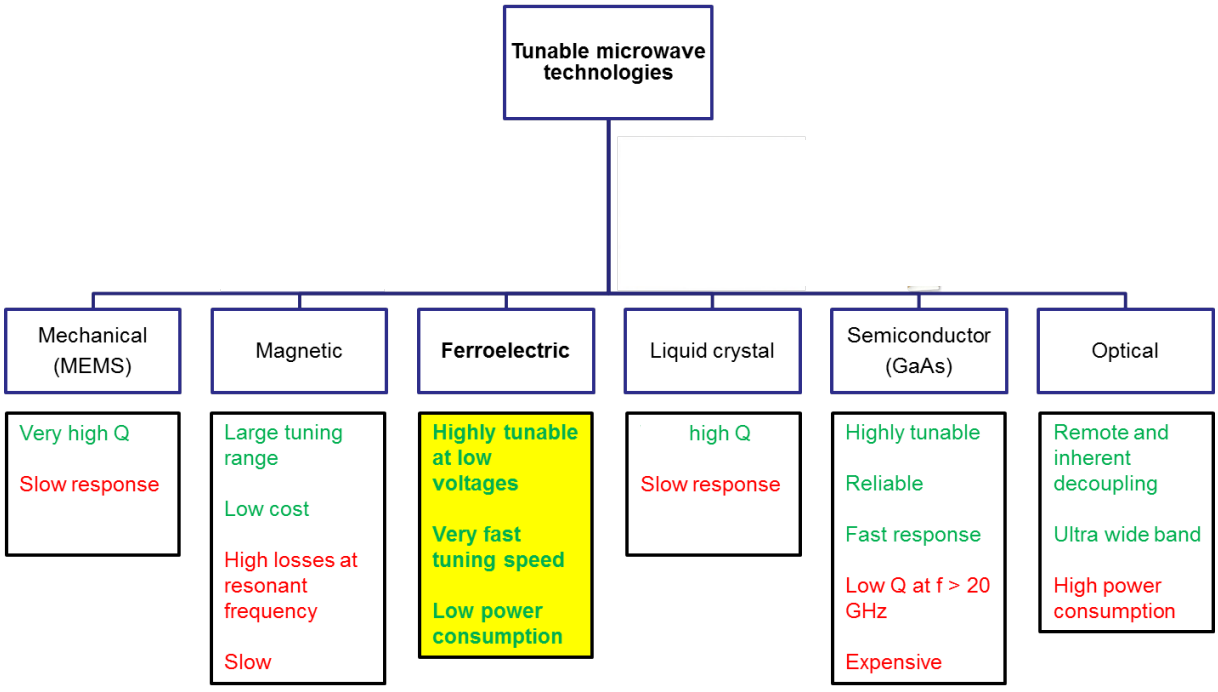

Fig. 1.1 Advantages and disadvantages of the most common technologies for production of varactors

Utilization of thin film ferroelectric materials in the fabrication of tunable capacitors offers miniaturization and low production and material cost [1], [3], [11]. Such varactors are used as an example to reduce the power consumption of antennas using matching networks based on thin film ferroelectric varactors [32]. Moreover, steerable antennas could exploit the potential of thin film ferroelectric varactors to save weight and space for satellite and space applications [33], [34].

Ferroelectric materials possess low dielectric losses at microwave frequencies and a strongly electric field dependent permittivity. Furthermore, the majority of the ferroelectric materials have a high permittivity at temperatures close to their Curie temperature. Several qualities of a dielectric material are of interest for applications in the microwave frequencies. The most important parameters for evaluation of the performance of ferroelectric thin-film varactors are discussed below.

The electric-field dependence of the permittivity is defined either as the *tunability* n or as the *relative tunability* n_{r} of a ferroelectric material. The tunability n is defined as the dielectric permittivity ε' in the absence of electric field (V=0) divided by the permittivity $\varepsilon'(E)$ under an electric field (E):

$$n = \frac{\varepsilon'(0)}{\varepsilon'(E)} \tag{1.4}$$

The *relative tunability* n_{r} is defined as the change of permittivity in an external field (E), divided by the permittivity of that material under no bias:

$$n_{\mathrm{r}} = \frac{\varepsilon'(0) - \varepsilon'(E)}{\varepsilon'(0)} \tag{1.5}$$

It must be noted that the permittivity is a complex quantity and in the 1.4 and 1.5, the ε' represents the real part of the permittivity.

Another important term in determination of the performance of a ferroelectric material in tunable varactors is the loss tangent $tan\,\delta\,(E)$. In general, the lower the loss tangent, the stronger is the dielectric response of a ferroelectric material to an external electric field. The loss tangent is calculated as the ratio of the imaginary part to the real part of the electric permittivity:

$$\tan\delta\,(E) = \frac{\varepsilon''(E)}{\varepsilon'(E)} \tag{1.6}$$

Another common term to describe the loss tangent is the quality factor Q:

$$Q = \frac{1}{\tan\delta\,(E)} \tag{1.7}$$

Generally, the dielectric materials in microwave devices are used in their paraelectric phase in order to avoid remnant polarization (hysteresis). It is generally observed that there is a trade-off between the loss tangent and the tunability of the BST thin films [11], [35]. Thus, depending on the application, a compromise on either higher tunability or lower loss tangent (high quality factor) has to be made. To be able to compare the performance of BST thin films, a figure of merit known as Commutation Quality Factor (CQF) is commonly calculated and referred to [36]:

$$\mathrm{CQF} = \frac{(n-1)^2}{n\,.\,\tan\delta_1\,.\,\tan\delta_2} \tag{1.8}$$

where n is the tunability defined in 1.4., $tan\,\delta_1$ and $tan\delta_2$ are the varactor loss tangent under no bias (V_1=0) and V_2 volts, respectively. While the CQF offers a measure to combine the loss tangent and tunability of a thin film varactor, it does not incorporate the absolute applied bias voltage which is an important factor for applications. In the literature, usually the total loss tangent of the device under test (DUT) is reported[11]. In certain cases, the loss tangent of the dielectric BST thin film is extracted from the total loss of the DUT [12], [20], [37]–[39].

While the former is of interest for device engineers, the latter helps materials engineers to evaluate the sole performance of the BST material for microwave applications [11].

1.3. Characterization of the dielectric properties

The most important parameters for evaluation of the dielectric properties of a material for integration into a microwave component are its permittivity, tunability, and loss tangent. Two types of capacitor structures are used for characterization of the dielectric response of ferroelectric thin films, namely the coplanar interdigitated capacitor and the parallel plate capacitor. A schematic of these two structures is illustrated in Fig. 1.2.

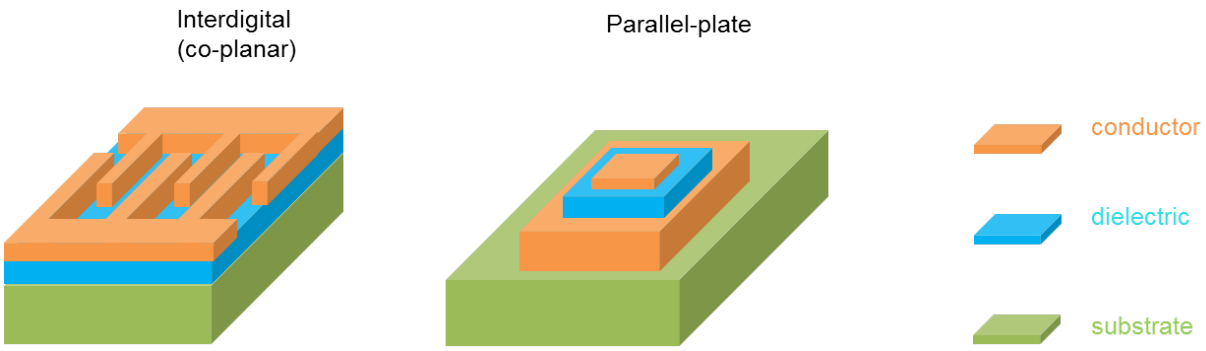

Fig. 1.2 schematic comparison of the varactors in co-planar and parallel-plate configuration

In general, fabrication of the interdigitated capacitors is simpler than that of the parallel plate capacitors. However, the electrode spacing in the interdigitated capacitors is usually in the range of few micrometers, limited by the resolution of the lithography. In the thin-film parallel plate capacitors, the distance between the bottom and the top electrode (dielectric thickness) is typically within the sub-micrometer range. Thus, by applying the same nominal voltage, the electric field in the parallel plate varactor would be much higher than that of the interdigitated capacitors. In general, lower tuning voltage requirement can result in a lower DC power consumption. Thus, considering the overall miniaturization trends in the Integrated Circuits (ICs) and also the global urge for lower power consumption in electronic devices, the parallel plate capacitors are becoming increasingly attractive.

For characterization of the dielectric properties of a ferroelectric thin film, different methods are employed to address these properties within the desired frequency range. High-frequency measurements usually differ from low-frequency measurements. At higher frequencies, there are several factors which must be taken into account. High-frequency measurements (GHz

frequencies) are typically done by means of a two-port vector network analyzer, which measures the scattering parameter (*S*-parameter) of the inserted waves into the test structure [40]. In this setting, the amplitude and the phase of the reflected and transmitted signals are measured.

Transmission line structures are a coplanar type of varactor used for characterization of materials at high frequencies (Fig. 1.3, top). Dimensions of CPWs are much larger than the microwave wavelength. Thus, *S*-parameter measurement of transmission lines is usually accompanied by electromagnetic simulations and equivalent circuit modeling. Typically, the signal line and the gaps are several tens of micrometers in width and few millimeters or more in length.

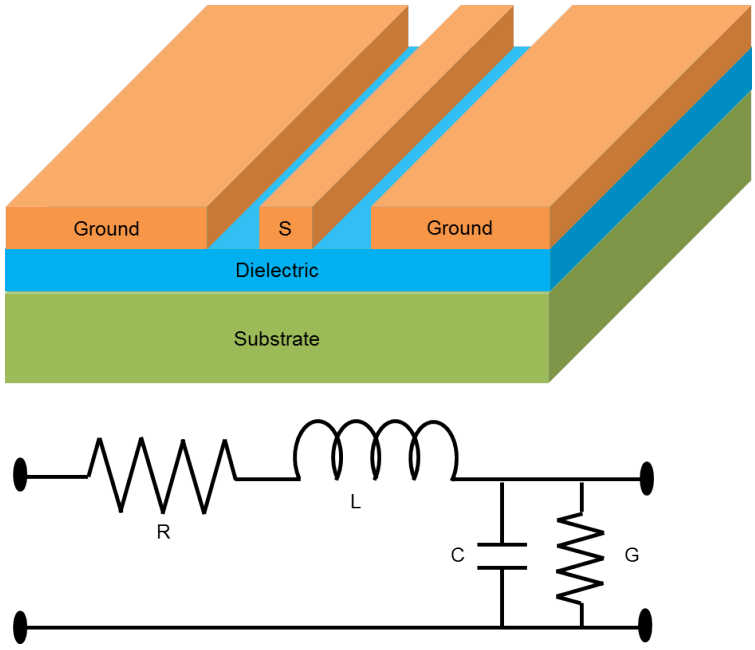

Fig. 1.3 Schematic (top) and the corresponding equivalent circuit (bottom) of a transmission line.

The width and the gap of CPWs are designed in a way that a total impedance of 50Ω is achieved, resulting in the reduction of the reflection of input signals[41]. The insertion loss, measured by the vector network analyzer, encompasses both the reflection loss and the attenuation due to conductor's and dielectric's loss. The *S*-parameter response of the coplanar transmission lines can be modeled using an RLGC transmission line (Fig. 1.3, bottom, where R represents the conductor's resistance, L is the inductance due to conductor's configuration, C is the capacitance, and G accounts for the dielectric loss). Utilizing the conformal mapping, the permittivity and loss tangent of the dielectric material can be obtained [11], [42].

In the parallel-plate structure, the parasitic resistances and inductances are much lower than that of the CPWs. Another advantage of the parallel plate test structures is that the electrode loss at small frequencies is negligible. Thus, the measured loss of the DUT can be regarded as the loss tangent of the dielectric material. Furthermore, for measurements at low frequencies, the pad size (top electrode size) is not a critical factor, resulting in a quick and easy processing and fabrication of the test structure. However, big pad (top electrode) size results in very low impedance at higher frequencies and causes short circuiting. Therefore, the size of the top electrode can be critical in the *S*-parameter measurement of parallel plate varactors at higher frequencies. On the other hand, minimizing the pad sizes is not only harder in terms of processing and fabrication, but also it is limited by the tip size of the conventional probes used for *S-parameter* measurement (typically few micrometers). Various circuit modelings and extraction methods of the dielectric loss have been studied so far [43]–[48]. Circuit modelings are usually used to remove the parasitic influence of the series resistance and also inductances. For characterization of thin film varactors, a simple MIM (Metal-Insulator-Metal) configuration is often employed (Fig. 1.4). The circuit model presented in Fig. 1.4 is a simplified equivalent circuit which ignores the capacitance of the substrate, skin depth of the bottom electrode, the resistance of the dielectric material, and the parasitic inductances between the top electrodes. In Fig 1.4, R_{t1} is the resistance of the top central electrode (signal pad), R_{t2} is the resistance of the top outer ring (ground pad), C_s is the capacitance of the dielectric material, proportionate to the area of the signal pad, R_b is the electrical resistance of the bottom electrode, and C_g is the capacitance of the dielectric material, commensurate with the area of the ground pad. The geometry of such a test structure is designed in a way that the outer electrode (ground) has a much larger area in comparison to the signal pad. This means that $c_g >> c_s$ and thus the influence of c_g is negligible. In the ideal case, the equivalent circuit model of such an MIM structure consists of subtle series resistances (total bottom and top electrode resistances) in series with the capacitance of the signal pad (Fig. 1.4, bottom-right).

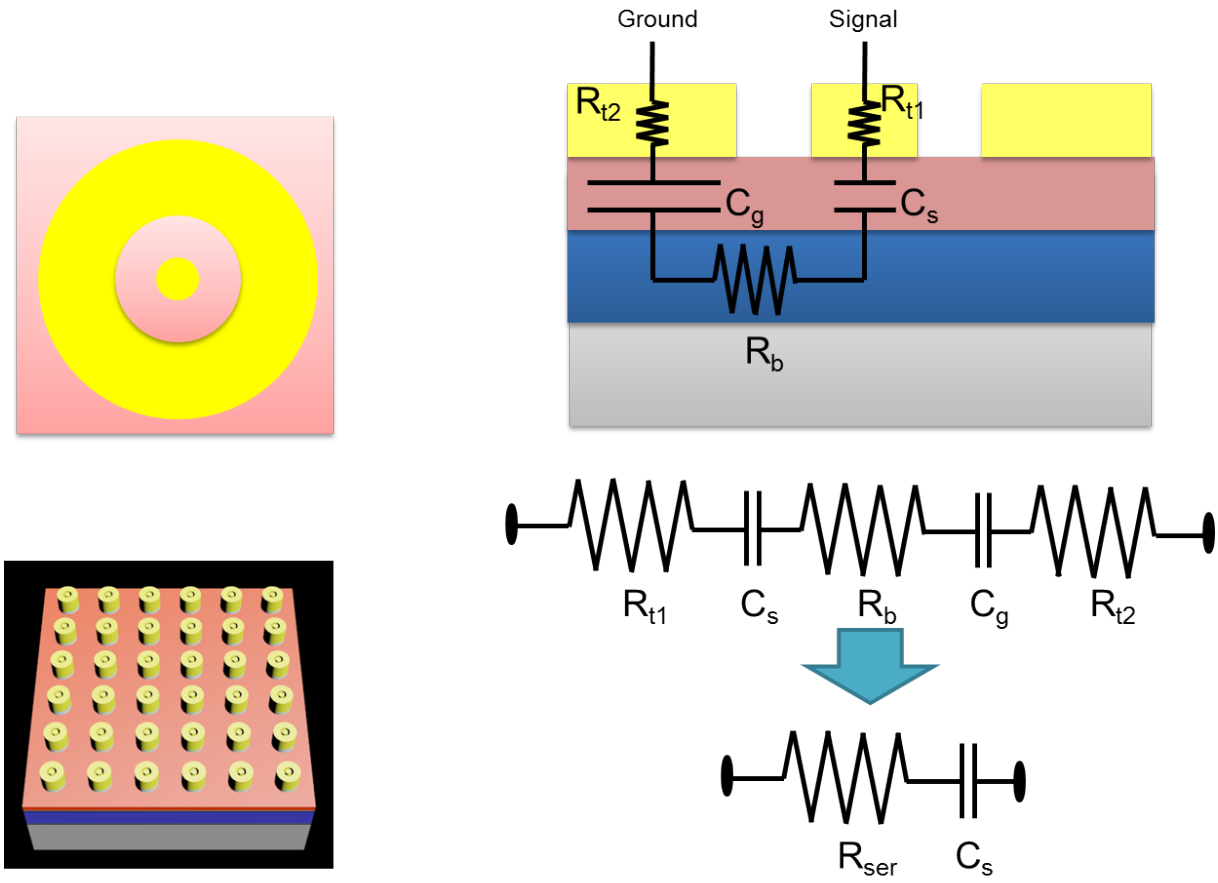

Fig. 1.4 Schematic of the top view of a parallel plate test structure (top-left), a typical sample with 36 test structures (bottom-left), the cross-section of a varactor (top-right) and its corresponding equivalent circuit (top and middle right). Bottom-right is the corresponding simplified equivalent circuit.

1.4. Barium Strontium Titanate (BST)

Barium Strontium Titanate $Ba_xSr_{1-x}TiO_3$ (BST) is one of the most promising and highly studied ferroelectric materials. BST has a perovskite structure and can be considered as a solid solution of barium titanate (BTO) and strontium titanate (STO), where Barium and Strontium are A-Site cations, titanium is the B-site cation, and oxygen anions shape an octahedral shell around the titanium (Fig. 1.5).

BST offers large dielectric constant (usually few thousands) near its Curie temperature. Moreover, the Currie temperature, crystal structure, and dielectric properties of BST are highly dependent on the ratio between Barium and Strontium (Hereinafter Ba/Sr ratio). Thus, BST offers a flexible performance range which serves the need for miniaturized microwave devices and components applicable at different temperatures and for various applications.

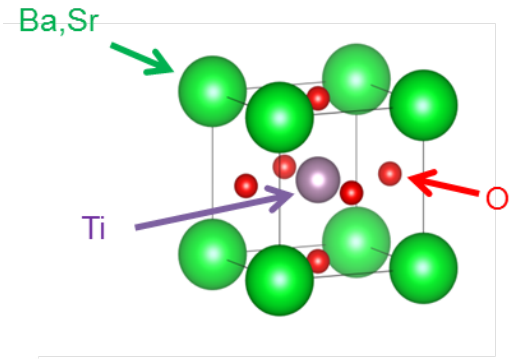

Fig. 1.5 Schematic of the perovskite crystal structure of the BST

The tunability, dielectric loss tangent, and commutation quality factor of BST thin films with 0<Ba/Sr<1 have readily been calculated [11], [49] and under the assumption of pure paraelectric behavior, the results of these calculations have been plotted (Fig. 1.6) [11].

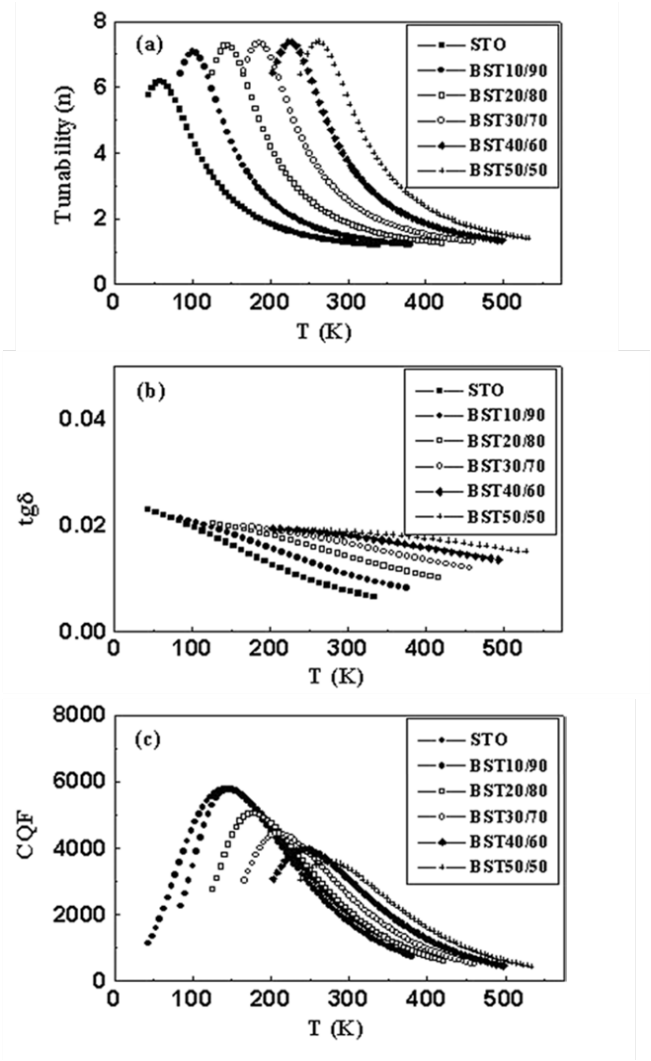

Fig. 1.6 The temperature dependence of the tunability, loss tangent, and commutation quality factor of BST thinfilm varactors, taken from [11], [49].

In Fig. 1.6, the *Curie temperature* of each composition is at the very left end of the tunability curve. Thus, it can be seen that the maximum tunability occurs around 10-20 degrees above the *Curie temperature*. Therefore, it is crucial to select the composition of the BST material with respect to the operational temperature. Moreover, it can be seen that at room temperature, an increase of the barium content to around 50% results in an increase of the dielectric tunability and also an increase of the dielectric loss tangent. Interestingly, the CQF also increases with the increasing Barium content, despite the increase of the dielectric loss tangent, due to the stronger impact of tunability in comparison to that of loss tangent in the CQF formula. Among other compositions, the $Ba_{0.5}Sr_{0.5}TiO_3$ (Ba/Sr =1) has the highest room temperature tunability and CQF. However, in thin films, effects from lattice strain, defects, and film inhomogeneity can shift the *Curie temperature*, tunability, and loss tangent values [50], [51]. Thus, it is important to characterize the BST dielectric properties in reproducible, simple, and comparable test structure configuration before integrating it into a final device. The most dramatic divide in the dielectric properties of BST thin films and the bulk BST of the same composition is the permittivity.

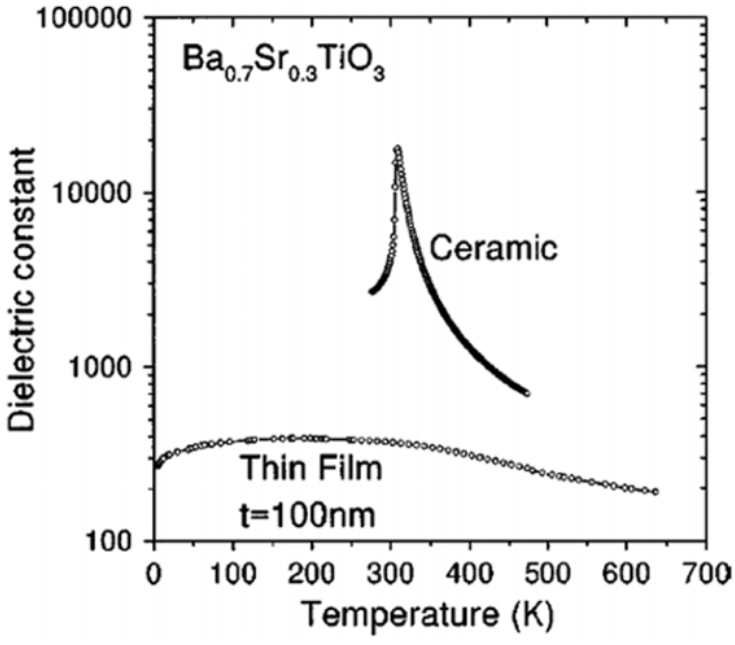

Fig. 1.7. Temperature dependency of the dielectric constant of a thin film and a bulk ceramic BST.

It has been observed that the dielectric constant of the BST thin film is significantly lower than that of the bulk BST. Moreover, the temperature dependency of the grown thin films is shown to be very different from that of the BST ceramics. As it can be seen in Fig. 1.7, the dielectric constant of the BST thin film is much lower than that of the bulk and exhibits no major peak at the phase transition temperature. This behavior has been attributed to the presence of defects[52], misfit strain[51], [53], dead layers at the interfaces[54], and local variations of the stoichiometry[11].

2. Growth and Characterization Methods

In this study, Pulsed Laser Deposition (PLD) was used for Heteroepitaxial growth of the thin film oxide layers. In section 2.1, the PLD method will be presented briefly. In section 2.2. fundamentals of the microstructural characterization techniques used in this study will be introduced. In section 2.3 a brief review of the patterning process for various electrical characterizations will be presented.

2.1. Pulsed Laser Deposition

This section encompasses a brief summary of the general aspects of the Pulsed Laser Deposition (PLD), with a focus on the available features of the PLD system used for this study.

PLD has widely been used for fabrication of high-quality thin films, in particular for conducting research on oxide materials[3], [55]. PLD offers a precise control of the growth conditions such as temperature, background pressure, and kinetics of arriving species on the substrate. Moreover, the growth of heterostructures consisting of several thin film layers makes PLD a good candidate for fabrication of multi-layer devices. In Fig. 2.1 a schematic of the PLD system used in this study is shown.

Initially, the desired material for deposition is pressed into a dense pallet (hereinafter called target). Target has a significant role in the film growth in particular for oxide materials [55]. Target needs to be dense to withstand the laser pulses without getting cracked and also to reduce the formation of the particulates during the ablation process. Moreover, the target needs to have a high absorption coefficient for the selected laser wavelength. Polycrystalline ceramics, due to their ease of preparation as well as high density and absorption coefficient, are the most favored target materials for the PLD process[56].

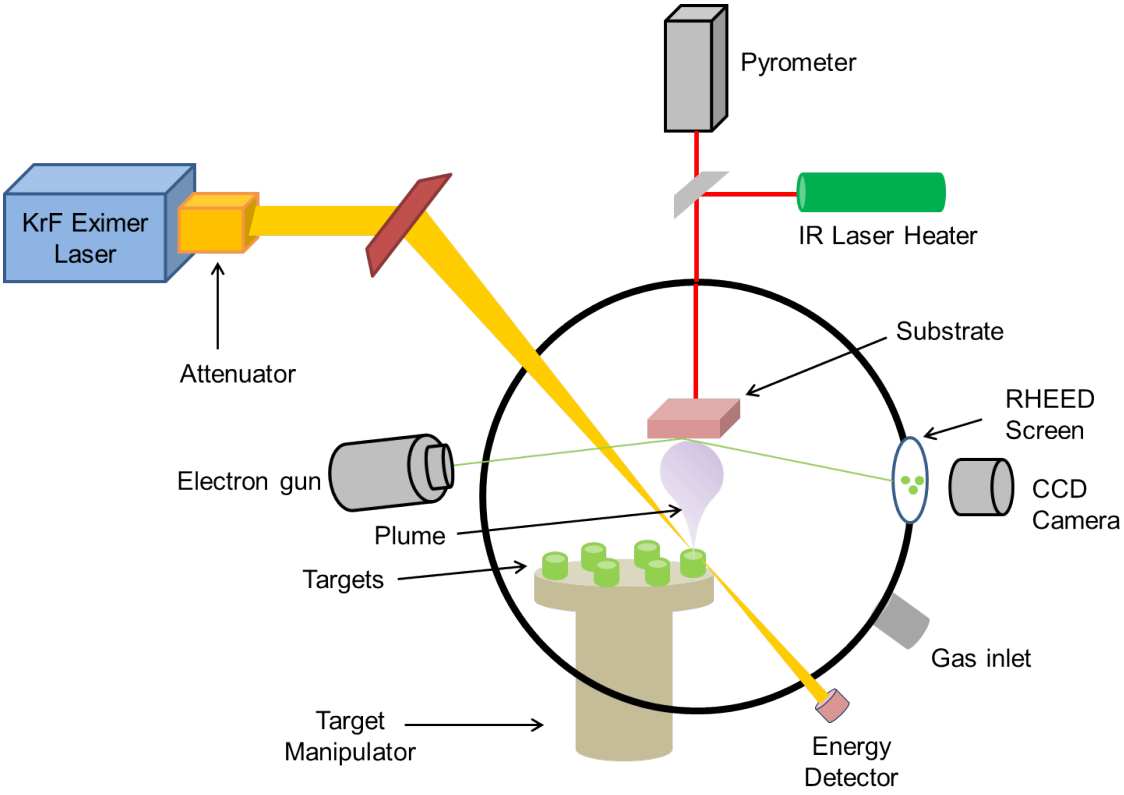

Fig 2.1. Schematic of the PLD system at the ATFT institute in the Materials Science department at the Technical University of Darmstadt.

The kinetic energy for transfer of the material from the target to the substrate is provided by means of a pulsed laser, focused on the surface of the target. Once the laser photons hit the target, two scenarios can occur. If the laser energy per area (J/cm^2), also known as laser *fluence*, is less than the binding energies of the atoms in the target material, the laser energy will be absorbed in the form of heat. This could result in vaporization of the target material. If the target material is evaporated, the stoichiometry of the species in the vapor phase would depend on their partial pressure, and thus a stoichiometric transfer of a multi-cation target material would prove difficult. Hence, the laser energy is selected in a way that it would exceed the binding energy of the atoms, also known as ablation threshold. Ablation is a process in which the laser pulse breaks the bonds of the target material and results in expulsion of the atoms. The ablation threshold depends on the absorption coefficient of the material which is a wavelength-dependent factor [55]. With higher laser energies, ejection of electrons at a supersonic speed takes place. By proper selection of the laser wavelength and laser pulse, high energy densities are absorbed by a small volume of the target material. Continuous rotation and sweep of the target material hinder local heating and unwanted evaporation of the target material. The ablation process forms an electric field which further

pulls the ions out of the target material. The ablated species form a plume. Depending on the laser fluence and pulse duration (usually in the range of tens of nanoseconds), the produced plume is a plasma-state containing atoms, electrons, ions, or molecules. In a dense plume, high interaction rate of the species results in a uniform cloud, extending towards the surface of the substrate.

Kinetics and thermodynamics of the arriving species on the surface of the substrate depend highly on the background gasses and their partial pressure. Interaction of the plume species with the background gas can be of both physical and chemical nature. An inert gas like Argon can be used to reduce the kinetics of the species. The Time-resolved spectroscopy studies of the ablation plume have shown that the kinetic energies of the arriving species on the surface of the substrate can reach 100 eV[56]. Such a level of energy is high enough to introduce defects in the film. In this context, background gasses are seen as a means to slow down the species on their way towards the substrate. Background gasses are not solely used for kinetics purposes. For example, insertion of oxygen molecules has been shown to assist the growth of oxide films such as BST. Interaction of the plume species and the oxygen molecules forms sub-oxide ions which facilitate the formation of the oxide phase in the deposited oxide layer[57].

The material ablated per pulse in the PLD process is usually not enough for the formation of a complete monolayer. Thus, through proper selection of the laser repetition rate (number of pulses per second), it is possible to control the growth at sub-monolayer scale, making PLD a viable technique for engineering of interfaces and deposition of multilayer thin films.

2.1.1. Thin Film Growth modes

Depending on the substrate temperature and the kinetic energy of the arriving species at the surface of the substrate, several scenarios are viable. Fig. 2.2. represent a schematic of these scenarios. The adsorption occurs when the arriving particles bond with the substrate atoms through Van-der-Waals forces. The landed particles might get reflected or desorbed by other particles on the surface. Furthermore, at higher kinetic energies, penetration of the arriving particles into the substrate material or inter-diffusion is also possible.

The nucleation process takes place when the particles agglomerate and form chemical bonds on the substrate surface. After nucleation, the growth of the material on the substrate can happen in a number of ways, depending on the surface energies of the substrate Γ_S, film Γ_F,

and the interface Γ_l. Young's equation rules the wetting of the substrate surface by incoming species:

$$\Gamma_s = \Gamma_1 + \Gamma_F \,.\, \mathrm{Cos}\,\theta \qquad 2.1$$

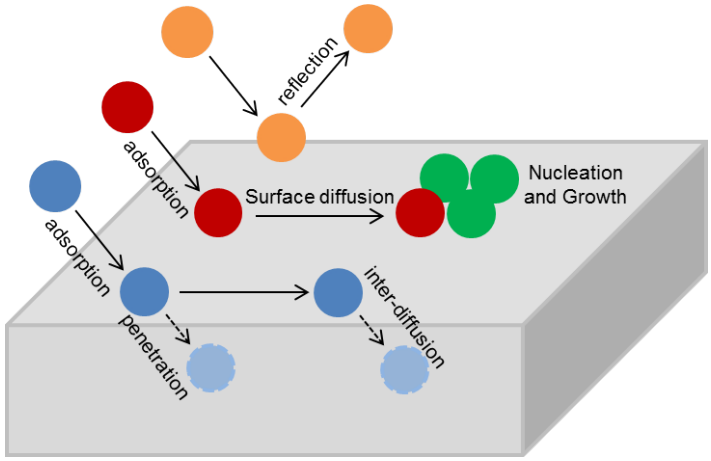

Fig. 2.2.Schematic view of the nucleation and growth scenarios

where θ is the contact angle. By assuming a spherical shape for the arriving atoms, the 2.1 is reduced to 2.2:

$$\Gamma_s = \Gamma_1 + \Gamma_F \qquad 2.2$$

The layer-by-layer growth mode, also known as Frank-van der Merwe, occurs when the total surface energy ($\Gamma_1 + \Gamma_F$) is lower than the surface energy of the substrate. In contrary, if the substrate energy is lower than the total surface energy of the film and interface, growth in the island mode, also known as Volmer-Weber mode, is favored.

A more complex scenario is the combination of the mentioned growth modes, where the initial growth is in the layer-by-layer mode, followed by a transition into island growth mode. Such growth is known as Stranski-Krstanov regime and usually, happens when the misfit energy increases upon film growth. Fig. 2.2 shows the schematic of possible growth scenarios.

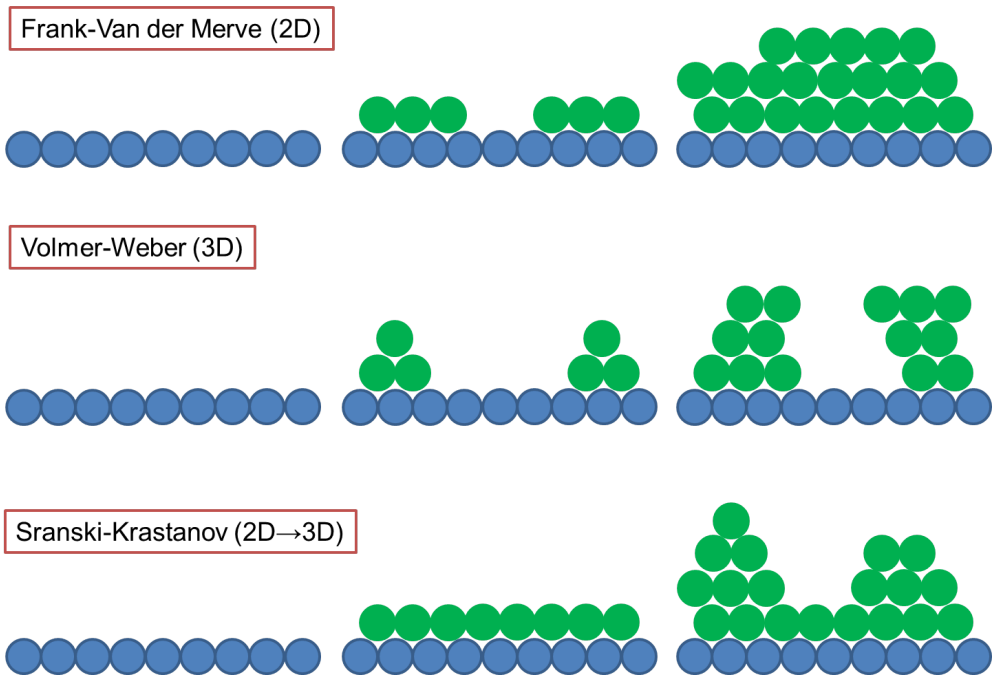

Fig. 2.2. Schematic of the possible growth modes of material on a substrate

2.1.2. Growth monitoring

Reflection High Energy Electron Diffraction (RHEED) can be used to monitor the growth of the thin film during the deposition (*in-situ*). The diffraction of the incoming electrons in a periodic lattice follows the *Bragg* equation in the reciprocal space. The grazing angle reflection exploits the forward scattering of high energy electrons by the crystal atoms. Thus, this technique is highly surface sensitive and can be used *in situ* to monitor the growth of the oxide crystals on a substrate. For a detailed explanation on the RHEED growth monitoring, please see [58].

2.2. Microstructural characterization methods

If the substrate and film material and structure are the same, then the growth process is called Homoepitaxy. When the substrate material differs from that of the growing film, then the process is known as Heteroepitaxy. Different modes of epitaxy may occur, depending on the geometric relationship between the film and the substrate. When the orientation of a thin film is preferential with respect to the crystallographic orientation of the substrate on which it is grown, the thin film is referred to as an epitaxial film. A higher degree of epitaxy is the lattice-matched epitaxy where the in-plane lattice of the film is nearly identical to that of the substrate. The commensurate mode occurs when the film lattice coincides in a one-to-one

manner on the substrate lattice. In this case, the film and substrate are regarded as commensurately locked to one another (Fig. 2.3, left). If the lattice points of the film coincide with some, but not all, of the substrate lattice points, then a coincident epitaxy takes place (Fig. 2.3, middle). The third type of epitaxy, known as Incommensurate mode, refers to a single crystalline thin film which effectively is without any grain boundaries, yet has no correlation with the lattice of the substrate. When the film grows, the misfit strain can result in the change of the lattice or introduction of dislocations. In this case, the film is relaxed meaning that the crystal lattice of the film would no longer accommodate the misfit strain and thus its crystal structure would become like that of the bulk material (Fig. 2.3, right)

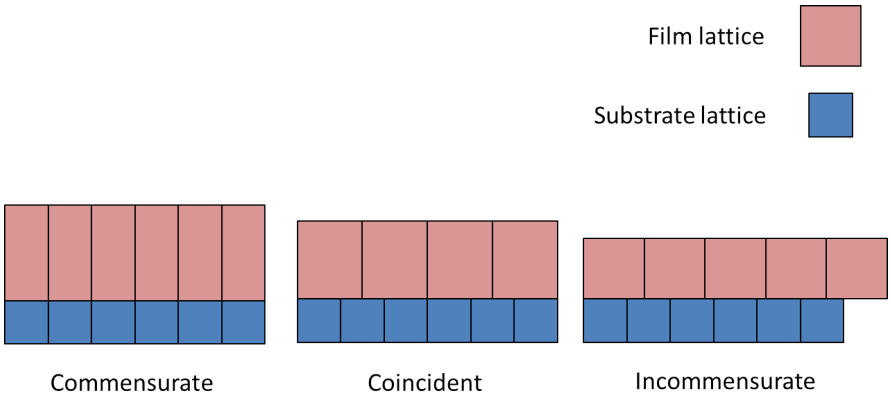

Fig. 2.3 Schematic of various heteroepitaxial growth modes of material on a substrate.

Commensurate heteroepitaxy under optimized deposition conditions brings about the in-plane lattice of the film being matched to that of the substrate. As a result, a strain in the unit cell is built up. Thus, in the case of an in-plane tensile or compressive strain, the out-of-plane lattice of the film will shrink or expand, respectively. Based on Poisson's formula, the conservation of the unit cell volume follows 2.3:

$$\mathrm{v} = \frac{\varepsilon_a}{\varepsilon_c} \qquad 2.3$$

where ε_a and ε_c represent the in-plane and out-of-plane strains, respectively.

For fully-relaxed films, the lattice parameters of the film are usually equal to the bulk values. If nucleation and growth of the thin film on the substrate would be favorable, crystals meet and bond perfectly, resulting in almost no grain boundaries. However, in reality, some of the nuclei are misaligned, resulting in low-energy, low-angle domain boundaries, known as mosaicity.

Mosaicity is caused due to the slight disorientation of the crystals as they nucleate and grow on the substrate. The microstructure of oxide thin films is known to have a significant impact on their physical properties [59]. Thus, it is crucial to monitor and engineer the crystal structure of the thin films to achieve optimal performances of these materials when integrated into a device. In order to characterize the microstructure of a thin film, several X-ray techniques are usually combined. In the following section the basics of X-ray characterization methods, used in this study, will be explained.

2.2.1. X-ray Spectroscopy

Interaction of X-rays with the electronic structure of the lattices in a condensed matter is the fundament of X-Ray spectroscopy. The electromagnetic waves of the X-rays possess a very short wavelength in the range of angstroms. When these waves interact with the matter, they can get scattered. X-Rays are also reflected, absorbed, refracted, or transmitted when they interact with matter. If the scattering is coherent, the wavelength and the energy of the wave before and after interaction remain identical[60]. Such a scattering is also known as elastic or Thompson scattering. In contrast to the Thompson scattering, if the wavelength of the scattered beam differs from that of the incident beam, an inelastic scattering happens. An inelastic scattering is also known as Compton scattering. Interference of the elastically scattered waves from crystal planes can result in the fulfillment of the Bragg's law (2.4). Such a scattering is known as diffraction. In other words, crystal atoms are a periodic array of coherent scatterers[61]. The strong intensity peak produced by the diffraction in a crystal is called the Bragg diffraction peak, fulfilling the Bragg's Law:

$$n\lambda = 2d_{hkl} \sin\theta \qquad 2.4$$

where λ is the X-ray wavelength, d_{hkl} is the distance between crystal planes in reciprocal space, and θ is the scattering angle. In the diffractometer, the λ is fixed. Thus, a family of planes, produce a diffraction peak only at a specific angle θ. The value of θ depends on the distance between the diffracting parallel planes. Based on the Bragg´s law and Laue equation, diffraction conditions are sensitive to stoichiometry and lattice spacing. Thus, X-ray studies are used for monitoring the stoichiometry and the crystallinity of the grown thin films. In the sections 2.2.1.1 to 2.2.1.3, the three methods of X-Ray diffraction spectroscopy, used in this study, will be introduced briefly.

2.2.1.1. Coupled scan ($\theta - 2\theta$ scan)

One of the most common arrangements is the out-of-plane $\theta - 2\theta$ measurement where the lattice planes parallel to the surface of the sample are investigated. Lattice mismatch, composition, and relaxation, all affect the position of the Bragg peak. Therefore, the $\theta - 2\theta$ measurement on an epitaxial film contains structural information on composition and thickness. Furthermore, the peak positions reveal the out-of-plane lattice parameters of the substrate and the deposited thin films.

The Bragg equation derives from the simplified interaction of the X-ray with one atom. In a crystal lattice, however, several scenarios may occur. Under the presence of defects in the crystal structure, one can assume that the incident x-ray is only scattered once by an atom. However, in the case of a defect-free crystal, the X-ray is scattered several times through the crystal structure. This process is called multiple scattering. In this case, the incident and diffracted x-rays in the crystal interfere with one another. Such interference is explained by the dynamical theory of diffraction which assumes that the intensity of the scattered x-rays drops due to absorption of the photons by crystal lattice. If the crystal structure grows in a layer-by-layer mode, the sequence of the crystal structure of the sample results in constructive interference of the incident and scattered waves, resulting in Laue fringes in the $\theta - 2\theta$ scan. Thus, presence of symmetric and sequential Laue fringes on both sides of the film peak in the 2θ-θ scan suggests a high degree of uniformity in the scanned area of the sample. The substrate and the film layers produce nearly separate plane waves. The interaction of the plane waves from the substrate and different layers of films produces additional peaks of intensity, also known as thickness fringes, which contains microstructural information. Fig. 2.4. shows an example of a $\theta - 2\theta$ scan, film and substrate intensity peaks, and thickness (Laue) fringes.

2.2.1.2. Rocking Curve (ω-scan)

If the nucleation and growth of the thin film on the substrate are ideal for epitaxial growth, the grown crystals meet and bond perfectly, resulting in almost no grain boundary creation. However, in reality, some of the nuclei are misaligned resulting in low-energy and low-angle domain boundaries, known as mosaicity.

Mosaicity is caused due to the slight disorientation of the crystals as they nucleate and grow on the substrate. The rocking curve measurement is usually employed to monitor the mosaicity in a crystal structure.

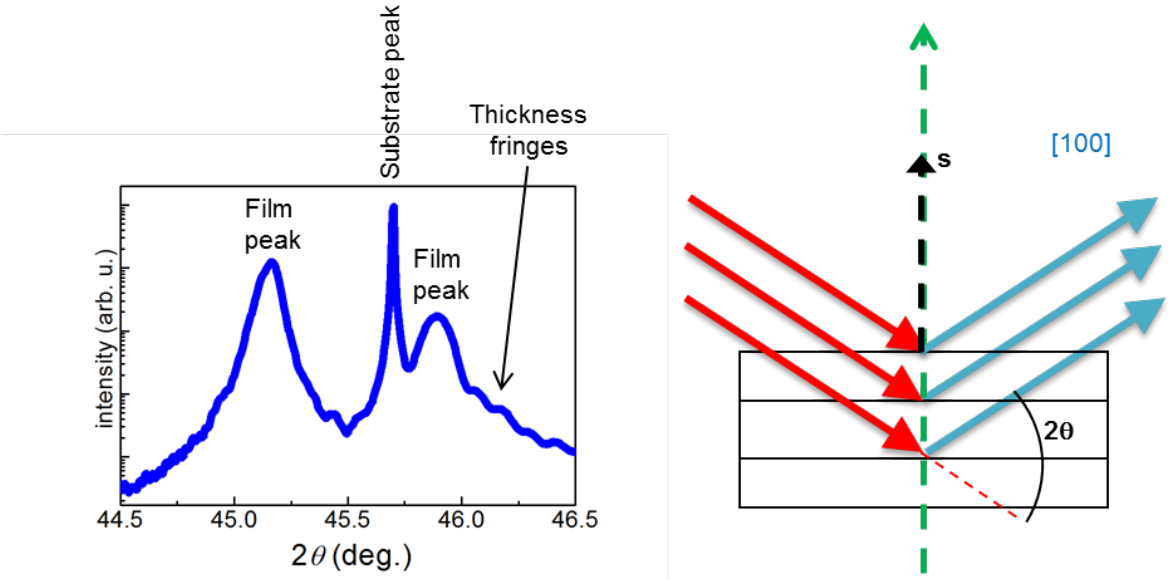

Fig. 2.4. An example of an XRD $\theta - 2\theta$ scan of epitaxial films on a single crystalline substrate, showing the films and substrate intensity peaks, and thickness fringes.

A Rocking Curve is a plot of X-ray intensity vs. slight change of Omega. Rocking curves are mainly used to study defects such as dislocation density, structural uniformity throughout the thickness (mosaicity), the curvature of the film, and inhomogeneity. In the case of epitaxial thin films, rocking curves are also used to study the layer thickness, superlattice periodicity, lattice mismatch, strain and composition profile, ternary compositions, and relaxation. In general, slip dislocations create a broadened rocking curve. Fig. 2.5 shows the schematic of the rocking curve measurement technique. Rocking curve measurement is explained in detail in [62], [63].

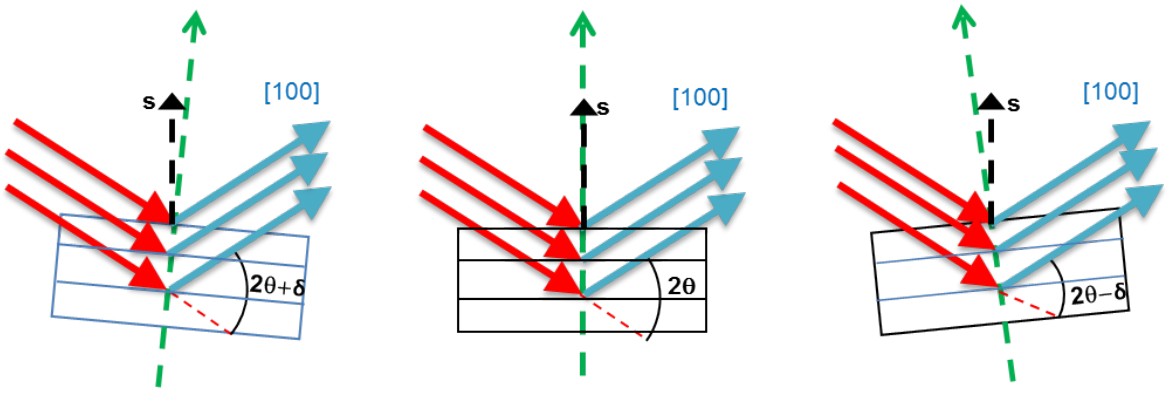

Fig 2.5. Schematic of the rocking curve measurement process

2.2.1.3. X-ray reciprocal space Mapping

Reciprocal space maps provide a complete set of information and are usually used to analyze strained films. The reciprocal lattice is a projection of the 3D crystal lattice to a 2D vector space where a vector represents each crystal plane. The reciprocal lattice vector $\vec{G}$ has a direction perpendicular to the plane that it represents in the real space. The spacing between the lattice planes is represented reciprocally by the length of the reciprocal lattice vector $\vec{G}$. In other words, diffraction follows the Laue equation (2.5):

$$\overrightarrow{k_f} - \overrightarrow{k_i} = \vec{G} \qquad 2.5$$

where $\vec{G}$ is the reciprocal lattice vector, $\overrightarrow{k_i}$ is the wave vector of incident x-ray, and $\overrightarrow{k_f}$ is the wave vector of the diffracted X-ray. The reciprocal space map uses multiple scans to observe both the film and substrate peaks. Maps of the symmetric Bragg peak can be used to separate tilts and strain. Reference [64] explains the reciprocal space mapping in detail.

2.3. Photo Lithography

Microlithography and Nanolithography are the technologies used to create patterns ranging in size from few nanometers up to tens of millimeters. Over the past decades, progress in patterning has sparked a rapid revolution in the semiconductor industry. The smallest features in integrated circuits (ICs) have scaled down to sub-micron sizes, enabling important functionalities of electronics, computers, and microelectromechanical devices (MEMs) [65]. Lithography techniques fall into two broad categories: masked and unmasked photolithography. The masked lithography is used to transfer patterns over a large area using a mask, resulting in quick and scalable fabrication process [66]–[68].

On the other hand, with the unmasked photolithography, it is possible to fabricate much finer structures. For example, it is possible to fabricate very small arbitrary patterns with focused ion beam lithography (FIB)[69], [70], electron beam lithography (EBI)[71], [72], or dip pen nanolithography[73].

Photolithography utilizes exposure of a light-sensitive organic material (called photoresist) to the ultraviolet (UV) light through a mask that consists of transparent and opaque features. In the case of a positive photoresist, exposure to UV light breaks the polymer chains and makes them soluble in the developer solution. Subsequently, the exposed features of the sample will dissolve in the developer, leaving the desirable pattern from the mask through the photoresist on the sample. One of the main methods used in photolithography to realize a pattern is to use the patterned photoresist to keep parts of a sample intact and leave the other parts uncovered. By using such a pattern, it is possible to etch away parts of a sample and leave the desired pattern of a thin film. The schematic of this process is shown in Fig. 2.6. After deposition of the desired film material on a substrate, the sample is cleaned. A layer of photoresist is then applied on the sample using a coating technology. Then the sample is heated so that the organics in the photoresist dry out to stabilize the photoresist on the sample. Then, using a mask, a pattern is transferred to the photoresist and the exposed photoresist is developed. After development, a brief O_2 plasma dipping can ensure that no residual photoresist remains on the parts which should have been removed by the developer. In this context, the photoresist is used as a covering layer to protect the areas of the sample which should not come into contact with the etching solution, ions, electron, etc.

After having patterned the photoresist on the thin film, the sample is etched using wet or dry etching. Wet etching refers to the chemical etching of a material with a chemically active solution or etchant. In this method, parts of the thin film which are not covered by the photoresist are etched away. A wet etching process usually involves series of reactions. Firstly, the etchant is diffused in or across the thin film. Then, some reduction or oxidation reaction happens between the etchant and the thin film material, followed by diffusion of the byproducts of the reaction from the reacted surface. Thus, stirring the etchant solution during the etching process is advisable. While the wet etching is generally isotropic, some dry etching techniques are also common, especially for anisotropic etching of the thin films. Dry etching requires ions, electrons, or photons with high energy to physically or mechanically remove the atoms from the uncovered thin film material.

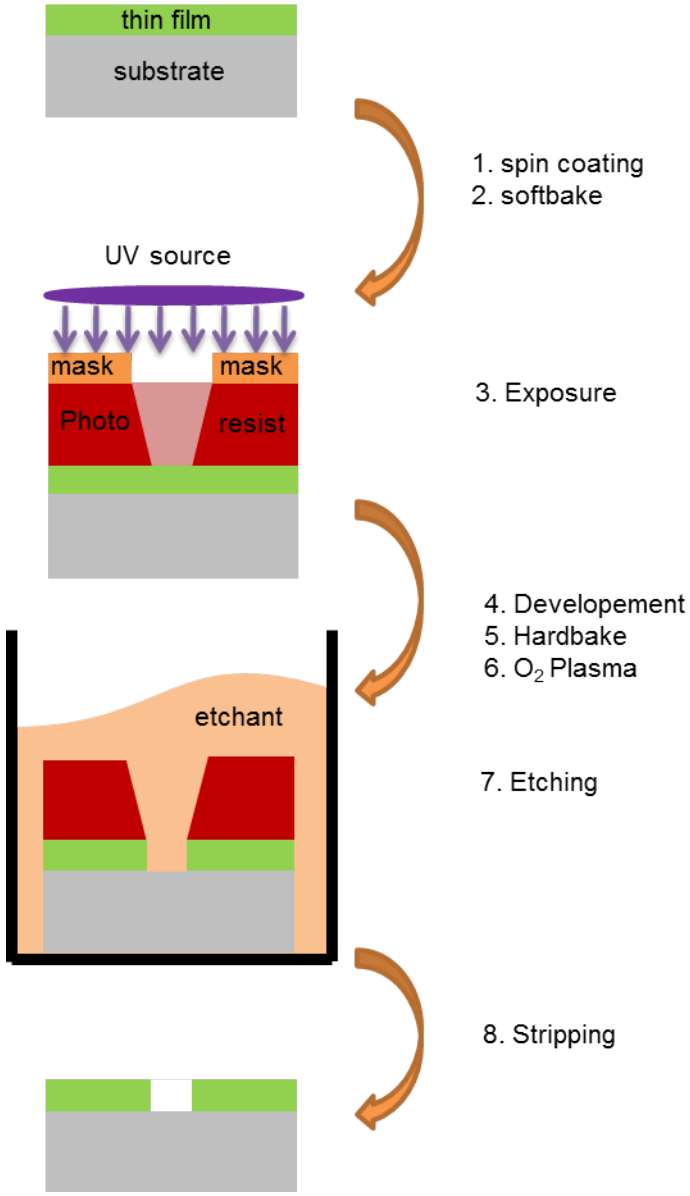

Fig. 2.6 Schematic and sequence list of the photolithographic steps used for etching.

If a chemical reaction occurs between the etchant and the thin film, the process is called chemical dry etching. Such a process is usually isotropic and shows high degrees of selectivity. Reactive Ion Etching (RIE) uses both chemical and physical mechanisms to achieve excellent resolutions.

Alongside wet or dry etching, lift-off is a standard technique to pattern metallic or oxide thin films in the micrometer and sub-micrometer range. In contrast to the etching methods, lift-off is a technique in which the photoresist is patterned and used as a mask to deposit material in the desired configuration on a substrate or thin film. Due to high resolutions of patterning of photoresist on the sample, it is possible to get very high resolutions after depositing another

layer(s) on the sample through the lithographic mask and lift-off process. The schematic of the lift-off lithography and its common sequence are shown in Fig. 2.7. After preparation of the desired substrate or thin film material on a substrate, the sample is cleaned. The cleaning process is usually done by acetone, provided that the substrate and the films be inorganic and acetone-resistant. A layer of photoresist is then applied on the sample using a coating technology. Then the sample is heated so that the organics in the photoresist dry out to stabilize the photoresist on the sample. Then, using a mask, a pattern is transferred to the photoresist and the exposed photoresist is then developed. After development, a brief O_2 plasma etching can ensure that no residual photoresist remains on the parts which should have been removed by the developer. In this context, the photoresist is used as a mask to protect the covered parts from subsequent depositions. Commonly, a physical vapor deposition (PVD) is used to deposit a material through the lithographic mask on the sample.

Some criteria are decisive in choosing the proper photoresist: thickness of the coated material, required resolution, available exposure wavelength, coating technology, and maximum temperature of the sample during the coating.

In general, positive photoresists are not suitable for lift-off process due to two reasons. Firstly, the softening point of the positive photoresists is around 110 °C to 130 °C. Typically, samples are heated to higher temperatures during the coating processes, and thus, the positive photoresist will soften and diffuse during the coating, making the lift-off process hard or even impossible. Secondly, the positive photoresist offers positive or 90° sidewalls, at best. Thus a full coverage of the photoresist during the coating makes the lift-off process hard or impossible. Thus, the lift-off process is usually done using negative photoresists.

Negative photoresists are typically designed to yield a reproducible undercut for the lift-off process. An undercut hinders the deposition of a film on the sidewalls and full coverage of photoresist. This facilitates the subsequent lift-off process (also referred to as “stripping”). Moreover, in the common negative photoresists, the crosslinking of the resins withstands the normal coating temperatures occurring during the physical vapor deposition (PVD) techniques. This maintains the undercut during the coating and thus facilitates the lift-off process.

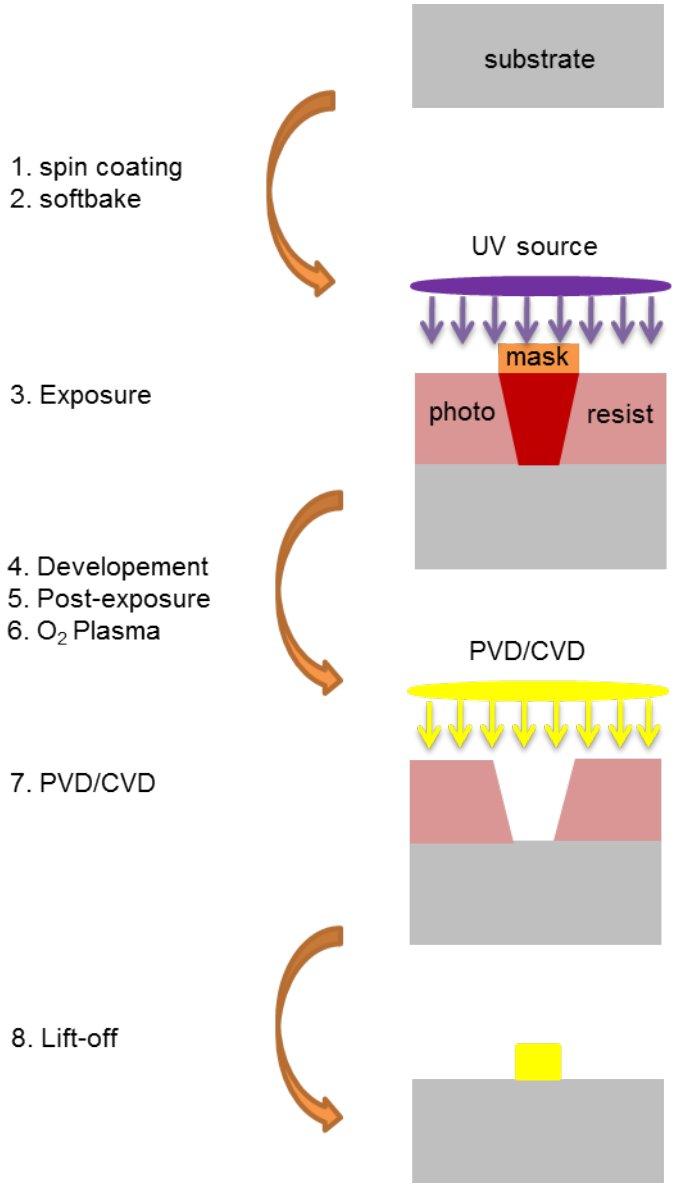

Fig. 2.7 Schematic and sequence list of the photolithographic steps used for lift-off lithography.

In the following sections, the lithographic steps will be explained briefly. These sections are a collective summary of parts of the reference: [65].

2.3.1. Choice of photoresist

The first step in photolithography is to coat the sample with a resist material. Photoresists need to be sensitive to the imaging radiation, offer a sharp edge profile after development, be etch-resistant, and be tolerant of variations in exposure levels. The required exposure depends on the sensitivity of the resist. Conventionally, exposure dose in milli-joules per centimeter

squared is provided by the producer of the resist [66]. Choice of the photoresist depends on the type of photolithographic process. Typically, for wet and dry etching, positive photoresists are used. For lift-off lithography, negative photoresists are more common. Depending on the type of photoresist, either the exposed part (negative photoresist) or the unexposed part (positive photoresist) will be resistant to the developer solution.

2.3.2. Photoresist coating methods

Spin coating, spray coating, dip coating, and roller coating is the four common methods used for distributing the photoresist on the substrate/film material. Table 2.1 summarizes the advantages and disadvantages of each technique.

Table 2.1 Comparison of common photoresist coating methods

Coating technique	*Advantages*	*Disadvantages/Limitations*
spin coating	• *thickness homogeneity* • *quick*	• *edge beads*
Spray coating	• *scalable* • *3D coverage*	• *high roughness* • *edge non-uniformity*
Dip coating	• *any shape, any size*	• *force rear-coating* • *too consumptive for lab-scale coating*
Roller coating	• *efficient*	• *sensitive*

The dip coating and the roller coating are mostly used for industrial and commercial applications. The spray coating is mostly used for obtaining 3D or angular coating of samples with spatial features. The most reliable, reproducible, and quick method for research is the spin coating. In this approach, the sample is placed on the spin coating holder where it will be sucked by vacuum to withstand the centrifugal force during the spinning. During the spin coating, a thin layer of photoresist coats the surface of the sample. By adjusting the speed of the spin coater (revolutions per minute) and the spin coating duration, the thickness and uniformity of the covering photoresist can be tuned. To have a clean surface for uniform

coverage of the sample with the photoresist, the sample is rinsed with acetone before spin coating, provided that the sample does not contain any organic or acetone-sensitive content.

2.3.3. Soft bake

The resist contains a residual solvent concentration (20-40%) depending on the type of resist, solvent, thickness, and the techniques used for coating. Conventionally, the spin coating is followed by a heating step also known as soft bake, to reduce the remaining solvent content. Softbake reduces the mask contamination, prevents foaming and popping of the resist during the exposure, improves the resist adhesion to the underlying layer, and prevents bubbling during subsequent thermal processes. Softbake can be done in an oven or on a heating plate. In the oven, the heat is transferred by convection rather than conduction. Thus, the sample is heated uniformly. However, the thermal hysteresis of the oven makes this method unsuitable for temperature-critical processes. In contrast to the soft baking in the oven, direct contact with the heating plate results in a quick baking of the sample. However, for thick layers of photoresist, heating the sample might lead to an over-baking of the closer layers to the substrate and under-baking of the top layers of the photoresist. This might affect the subsequent development rate of the photoresist after exposure. The soft bake time and temperature need to be tuned. A soft bake too short or too cold can cause foaming and bubbling during the exposure, whereas a soft bake too long or too hot can result in cracks in the photoresist film or decomposition of the photo-active compound and thus lower development rate. As a rule of thumb, per final µm thickness of the photoresist a minute of soft-baking at around 100 °C is common. A precise adjustment of the soft bake time and temperature is necessary for fine-tuning the final resist structure, undercut angle and shape, and surface roughness.

2.3.4. Exposure

Typically, coating the sample with photoresist and soft baking follows by exposure to the ultraviolet (UV) lamp. To precisely transfer the pattern from a mask to the light-sensitive photoresist, the alignment and subsequent exposure of the sample is performed by a single device called *mask aligner*.

After aligning the photo mask on the sample, the mask is pressed on the sample. In the soft contact mode, the substrate is brought into contact with the mask by a mechanical force. In the hard contact mode, the substrate is also pushed with a pillow pressure of Nitrogen,

resulting in additional upward force to the sample. A vacuum seal between the sample chalk and the mask can result in a vacuum contact mode which hinders alignment shift during the deposition.

Typically, the emission spectrum of a mask aligner with Hg source contains g-line (λ=436 nm), h-line (λ=405 nm) and i-line (λ=365 nm). A calibration of the illumination intensity is done for processes sensitive to exposure dose, such as thick resist processing or processes with sub-micron resolutions. The optical absorption of most of the photoresists ranges from 440 nm to near UV which matches the emission spectrum of the Hg lamps. A thin photoresist (less than 1-2 µm) is homogeneously exposed from the beginning of the exposure. Thus, increasing the exposure dose does not necessarily increase the development rate. In contrary, for thicker photoresists (few micrometers), the light will first penetrate the first 2-3 µm of the film and gradually penetrate deeper. Thus, the exposed (and later developed) resist film thickness is approximately linearly proportionate to the exposure dose. The photoresist manufacturer usually provides the required exposure doses for various photoresists. A typical 1000 W bulb, for example, achieves a light intensity of approximately 60-90 mW/cm^2 over g-, h-, ad i-line, with an i-line fraction of about 30% of the total intensity. As a rule of thumb, for most positive resists the optimum exposure dose results in saturation of the development rate. For negative resists, the proper dose depends on the required degree of cross-linking and the preferred sidewall resist profile.

2.3.5. Development

Once exposed, the photoresist needs to get developed. The developer removes the exposed part of the photoresist if a positive photoresist is used. In contrary, if a negative resist is used, the exposed parts will become insensitive to the developer. Alkaline developers develop most of the commonly used resists. Development is one of the critical steps in photolithography when an undercut for the lift-off process is required. The interaction chemistry and kinetics between the developer and the photoresist are decisive in the shape of the photoresist profile. Conventionally, after the exposure, the sample is dipped in a beaker containing the developer solution, usually with some agitation. In the industrial scheme, other development configurations such as spin or spray development have become prevalent. The sample (usually a wafer in an industrial setting) is typically spin dried after the development.

2.3.6. Hard bake

Hardbake is an optional step after the development which reinforces the thermal, physical, and chemical stability of the developed resist structure and prepares it for subsequent deposition or etching. A hard bake step bolsters the resist adhesion to the substrate. This is, in particular, necessary for subsequent etching processes. However, chemical stabilization of the photoresist by hardbake usually follows a strenuous removal of the resist at the end of the lithographic process. Therefore, hardbake can usually be avoided by optimum substrate pre-treatment and selection of the proper photoresist.

In the case of negative photoresist, flooding of the sample with UV light (also known as post-exposure) is a common alternative for hardbake, resulting in further hardening of the photoresist after the development process.

3. Sample preparation

In this chapter, the experimental process for fabrication of the samples will be explained.

3.1. Choice of substrate

BST has been shown to grow epitaxial on a broad range of substrates, including metalized substrates, silicon wafer, and oxide single crystal substrates[56], [74]. In an industrial setting, a low-cost, thermally stable, low insertion loss, and chemically resistant substrate would be interesting[3]. However, the substrate material and its crystal structure can have a direct influence on the physical properties of the film which is deposited on it. Thus, selection of the substrate is necessary not only for commercialization of the technology but for the following reasons:

Firstly, in commensurate thin films, the internal stress and strain, induced by the substrate lattice, result in lattice strain in the deposited films. The strain in the thin film affects the soft phonon mode which in return influences the dielectric constant of the ferroelectric material. Furthermore, the lattice misfit between the substrate and the thin film at the deposition temperature results in misfit strain. Such a strain can be relieved by nucleation and propagation of misfit dislocations during the growth. In general, fully strained films are usually expected at slight mismatch of less than 1% [11]. Fig. 3.1 shows the lattice parameters of conventional oxide perovskite materials and rare-earth scandate substrates, within the limits of the $BaTiO_3$ and $SrTiO_3$ lattice constant.

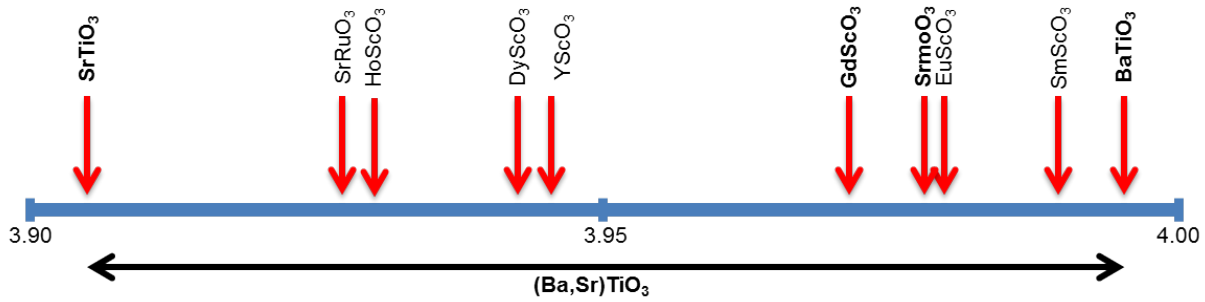

Fig. 3.1 Pseudo-cubic lattice constants of the rare-earth scandates, oxide perovskites, and perovskite-related structures at room temperature, taken from [75].

Secondly, the substrate-film interface plays a major role in the properties of the deposited film. As an exmple, a chemical reaction between the substrate material and the deposited

layer can result in an unwanted dead layer which could negatively affect the physical properties of the deposited layer.

Thirdly, for applications at microwave frequencies, the dielectric loss and permittivity of the substrate material should be as low as possible.

Thermal expansion coefficient of sputtered BST is reported to be between 7.8 E-6 to 11E-6, depending on the Ba/Sr ratio [76]. In Table 3.1, the most common substrate materials of choice and their related properties are listed. The only substrates which fulfill all the three above-mentioned criteria above are $GdScO_3$ and the $DyScO_3$. To minimize the misfit strain between the substrate and the $SrMoO_3$, the single crystalline (110) $GdScO_3$ was used in this study as the substrate material. The commercially available 1mm thick orthorhombic $GdScO_3$ (GSO) with lattice parameters a=5.482A, b=5.742A, and c=7.926A with a pseudocubic in-plane lattice parameter of 3.967A were purchased from Crystec GmbH.

Table 3.1 Physical properties of conventional substrate materials and their lattice mismatch with $SrMoO_3$. [11], [75], [77] blue means suitable, red means not suitable, and yellow means hardly suitable.

Substrate	Si	$DyScO_3$	$GdScO_3$	$LaAlO_3$	LSAT	Al_2O_3	$SrTiO_3$	MgO
Crystal structure at room temperature	Cubic	Orthorhombic	Orthorhombic	Cubic	Cubic	Hexagonal	Cubic	Cubic
Lattice parameter a	0.543	0.554	0.545	0.382	0.387	0.476	0.391	0.421
Lattice parameter b	0.543	0.571	0.575	0.382	0.387		0.391	0.421
Lattice parameter c	0.543	0.789	0.793	0.382	2.3	1.3	0.391	0.421
Lattice mismatch with $SrMoO_3$ %	3.9	0.4	0.2	3.6	3.6	16	1.2	6
Relative permittivity	≈12	≈21 @1MHz	≈21 @1MHz	≈25	≈22	9.4/11.5	≈300	9.8
Dielectric loss tan δ (at 10 GHz)	≈2E-4 [77]			≈3E-4	≈2E-4	<5E-5	<5E-4	<2E-5
Thermal expansion coefficient	3.6 E-6	8.4 E-6	10.9 E-6	11 E-6	10 E-6	7.3 E-6	9.4 E-6	12.8 E-6

3.2. STO buffer layer

Unlike stable materials, the growth of metastable materials like $EuMoO_3$ has proven difficult on the single crystalline $GdScO_3$ substrate [78]. It has also been shown that a thin (5nm) interlayer of a stable material such as $SrTiO_3$ can enhance the crystal quality of the $EuMoO_3$ deposited on the $GdScO_3$. This is claimed to be mainly due to the valance-mismatched interface effect. When $La^{3+}Al^{3+}O_3$ is grown on $Sr^{2+}Ti^{4+}O_3$, electronic reconstruction results in a partial reduction of the Ti^{4+} to Ti^{3+}. Although the $Sr^{2+}Ti^{4+}O_3/Gd^{3+}Sc^{3+}O_3$ may suffer from the energetically unfavorable interface with the GSO, the thermodynamic stability of the STO can better handle this electronic reconstruction. The deposited STO layer on the substrate provides a smooth transition from the pseudocubic substrate to the cubic SMO film Details of this study will be published elsewhere.

In this work, five monolayers of STO were deposited on the GSO substrate. The deposition was done in Ultrahigh Vacuum (UHV, 10^{-8} Torr) using PLD. Laser energy of 0.5 J/cm^2, laser repetition rate of 2 Hz, and a substrate temperature of 630°C were used to deposit the initial STO layer on the GSO substrate. As it can be seen in the RHEED oscillation spectrum (Fig 3.2, left) in the first 10 seconds of the deposition, the reflection intensity falls sharply. However, after about 10 seconds, the RHEED intensity quickly recovers, and the oscillation becomes pronounced, suggesting a layer-by-layer growth of the STO. The STO deposition is terminated after 5 unit cells are grown, namely, after five intensity oscillations in the RHEED pattern is completed.

Bright-Field scanning transmission electron microscope (STEM) images of the GSO/STO interface (Fig. 3.2b) show the epitaxial relation of the STO layer grown on the GSO. In the first 10 seconds of the deposition, misfit dislocations are nucleated on the STO layer to relieve the misfit strain, induced by the substrate lattice. This observation confirms the reconstructive role of the STO as a buffer layer on the $GdScO_3$.

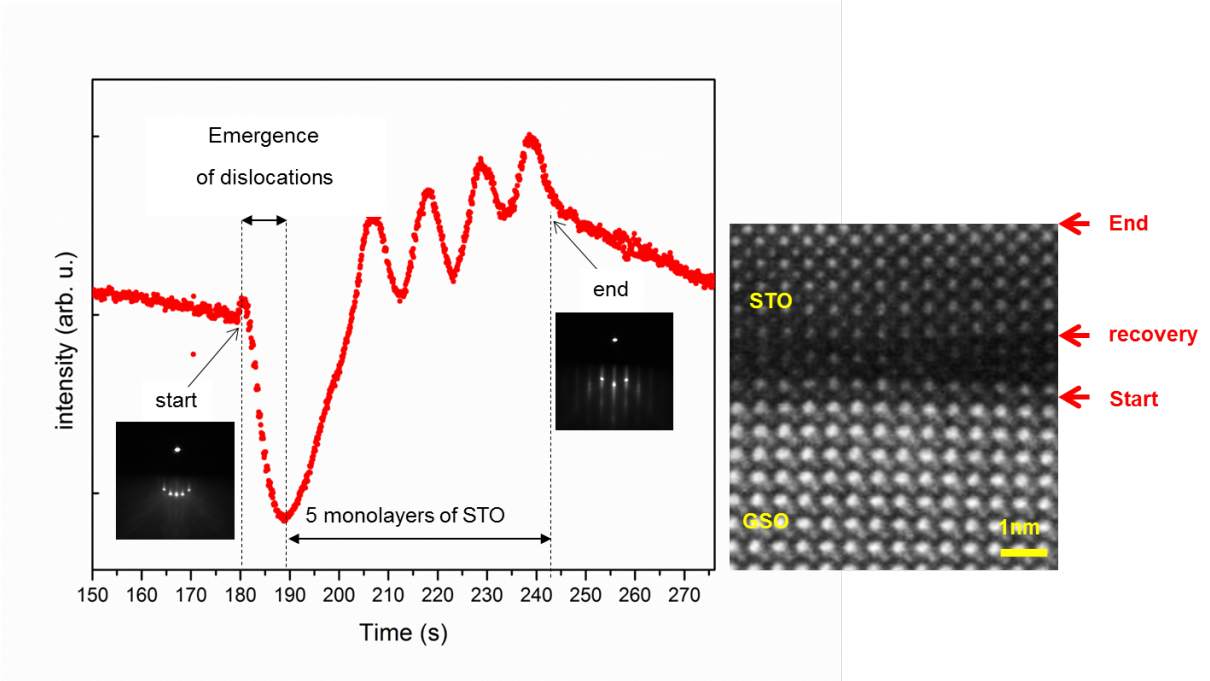

Fig. 3.2 Intensity of the RHEED specular spot during growth of the STO layer on the GSO (left) and the STEM image of the GSO/STO interface (right)

3.3. $SrMoO_3$ bottom electrode

Among all known perovskite oxide materials, $SrMoO_3$ (SMO) is shown to have the lowest electrical resistivity (5.1 μΩ.cm) at room temperature [6], [79], [80]. For using SMO as the bottom electrode, one needs to grow a thick layer of this material in order to achieve low electrical resistivity. On the other hand, it is important to keep the epitaxial relation of the SMO to the substrate and prevent relaxation. Thus, it is crucial to grow thick SMO bottom electrodes which are fully strained and locked commensurately to the substrate. It is also important to have a smooth surface for the successive deposition of the dielectric BST layer on top of the seed SMO layer. Most importantly, $SrMoO_3$ is a metastable material which, in the presence of oxygen or air, can easily get oxidized to the insulating $SrMoO_4$. Thus, it is also critical to prevent the oxidation of SMO during the deposition of the BST layer and the processing of the sample.

In previous work by Aldin Radetinac, deposition of a smooth and epitaxial SMO using PLD was established[6]. To use the SMO as a bottom electrode for varactors with applications at microwave frequencies, it was crucial to assess the electrical properties of the SMO in the DC as well as at the microwave frequency range. Results of this study have been published in [7]. It was shown that SMO thin films possesses a constant microwave resistivity of 29 μΩ·cm between 0.1 and 20 GHz, making it an excellent candidate for microwave applications.

In this wok, a KrF excimer laser at 248 nm wavelength was used to ablate a dense $SrMoO_4$ target material. A fluence of 1.5 J/cm^2, laser repetition rate of 4Hz, and a background gas of 2.5% H_2 in Argon at a pressure of 50 mTorr was used to deposit the SMO on the (110) GSO substrate. The STO buffer layer was used for better crystal quality and a smoother surface, as described in the previous section. *Insitu* RHEED was used to monitor the growth mode and the growth rate of the SMO layer throughout the deposition. An excellent crystal quality of epitaxial SMO up to 391 nm thickness was achieved. Results of this study are published in [7].

3.3.1. SMO etching

To be able to characterize the electrical properties of SMO at microwave frequencies, the scattering parameter measurement of the SMO CPWs was used. Fabrication of the SMO CPWs requires structuring the SMO either using a shadow mask or by etching. The lift-off technique cannot be used at the deposition temperature of SMO, around 600°C, due to the volatility of the photoresists. Shadow masking also results in a broad edge profile and disturbs the epitaxial growth of the SMO film and also hinders the *in situ* RHEED monitoring, necessary for the growth of high-quality SMO thin films.

Among the possible etching options, the ion milling is conventionally used to pattern oxide thin films, resulting in sub-micrometer resolutions. Not only is the ion milling expensive and time-intensive, but also it does not suit the patterning of a meta-stable material such as SMO. In contrast, wet chemical etching is a low-cost method which is easily scalable for future large-scale fabrications. More specifically, if the wet etching is properly tuned, it can result in a selective etching which could be of particular advantage for device fabrication. Thus, in this work the etching rate of the SMO using various etching solutions was investigated.

Typical etchants for oxide materials include a broad range of solutions, namely acids, bases, and (in)organic ligands. In the case of SMO, the multiple valence states of the Molybdenum can result in a controllable and selective etching. In the presence of oxygen, the meta-stable SMO ($SrMoO_3$) oxidizes to the stable $SrMoO_4$. However, the physical properties of the $SrMoO_4$ differ from that of the SMO significantly. Thus, it is important to bear in mind the sensitivity of SMO to oxygen and air throughout the fabrication and processing steps.

In this work, systematic etching of the SMO using alkaline solutions was studied. Furthermore, controllability, selectivity, and the etching rate of the etching process were evaluated.

Epitaxial thin film SMO was grown on the 5x5mm (110) $GdScO_3$ substrate, as explained in section 3.3.1. The crystalline quality of the deposited thin film was analyzed using X-Ray diffraction methods, explained in 2.2.1.

To lower the impact of crystal quality on the etching rate test, only one sample was used for all the etching study and later on other samples were tested by the same etchants to assess the reproducibility of the results. Thus, in each etching step, the sample surface was covered by a 5µm-thick photoresist (AZ6632, commercially available from Michrochemicals), except for a small window which was kept open for the etching (see Fig. 3.3)

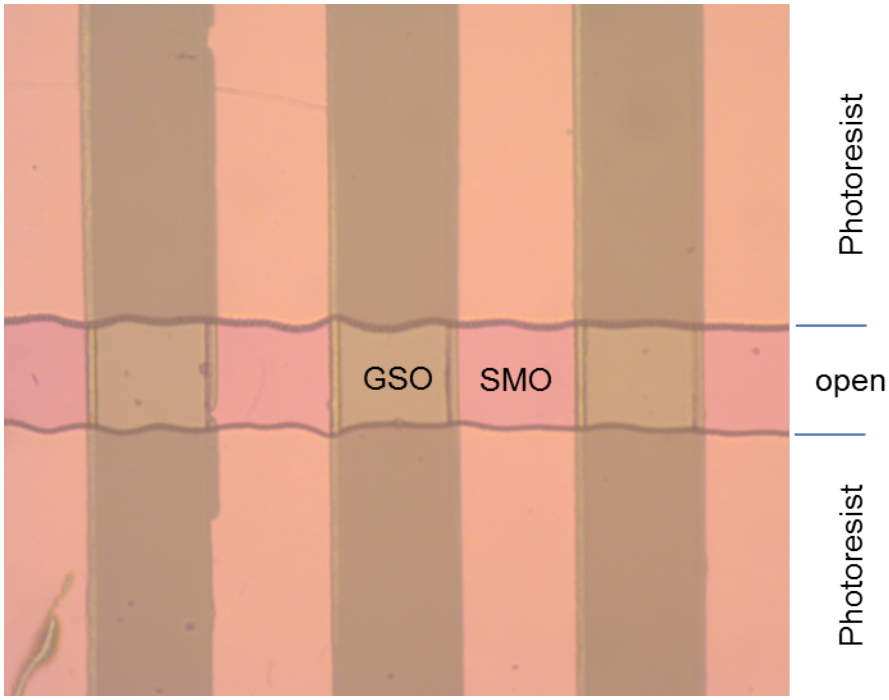

Fig 3.3 Optical image of the sample with $SrMoO_3$ thin-film stripes (pink); horizontal window is opened in photoresist for etching of the $SrMoO_3$ film;

Each etching step was done for 30 seconds, followed by rinsing the sample in the deionized water. After each etching step, the thickness of the SMO film was measured by a Dektak Profilometer. Some of the used etchants also etched the surface of the photoresist. Thus, the Photoresist/SMO edge height could not be the right measure for evaluating the etching rate of the SMO. Therefore, the SMO film was firstly patterned into stripes, so that the perpendicular

design of the photoresist's opened window on the SMO stripes would allow the use of the substrate surface as the height benchmark for thickness measurements. In a quick experiment it was made sure that the GSO substrate surface was not affected by the alkaline solutions which were used as etchants in this study. The etching steps were repeated until the SMO layer was completely removed. Then the photoresist was removed by acetone and adjacent intact part of the sample was used similarly for testing of other etchants.

To select the right etchants, chemical properties of the SMO need to be understood. The SMO consists of strontium and molybdenum oxides. The strontium oxide is of highly basic nature, which in the presence of water forms strontium hydroxide, barely soluble in the alkaline media. In contrast, the solubility of molybdenum oxides depends on the pH of the solution and the oxidation state of the molybdenum. In general, Acidic solutions do not react with the molybdenum oxide. In order to confirm this, etching of the SMO sample with the nitric acid was performed. At low acid concentrations, the film could not be etched, as expected. It was only at very high nitric acid concentrations of about 60% that an immediate and prompt dissolution of the SMO in the etchant was observed. However, the rate of the dissolution was not controllable, mainly due to the formation of Sr^{2+} and isopoly molybdate in the highly acidic environment.

To disintegrate and dissolve the $SrMoO_3$ it is necessary to understand the behavior of the multivalence molybdenum. In the presence of oxygen, the low-valent Mo^{4+} tends to get oxidized to the Mo^{6+} (MoO_3). The hexavalent molybdenum then reacts with the neutral or alkaline environment to form molybdate.

$$MoO_3 + 2\ OH^- \rightarrow [MoO_4]^{2-} + H_2O \qquad 3.1$$

Thus, the SMO in contact with an alkaline solution undergoes the following reactions.

$$SrMoO_3 + 0.5\ O_2 \rightarrow SrMoO_4 \qquad 3.2$$

$$SrMoO_4 \rightarrow Sr^{2+} + [MoO_4]^{2-} \qquad 3.3$$

If such a mechanism is valid, then the surface of the SMO film in the presence of oxygen, oxidizes first to the $SrMoO_4$ and only then the $SrMoO_4$ will get dissolved in the alkaline

solution. To evaluate this hypothesis, the H_2O_2, which is an oxidizing agent, was added to the tested etchant solutions to check whether enhanced oxidation might result in a quicker etching process. A schematic view of the proposed etching mechanism is shown in Fig. 3.4

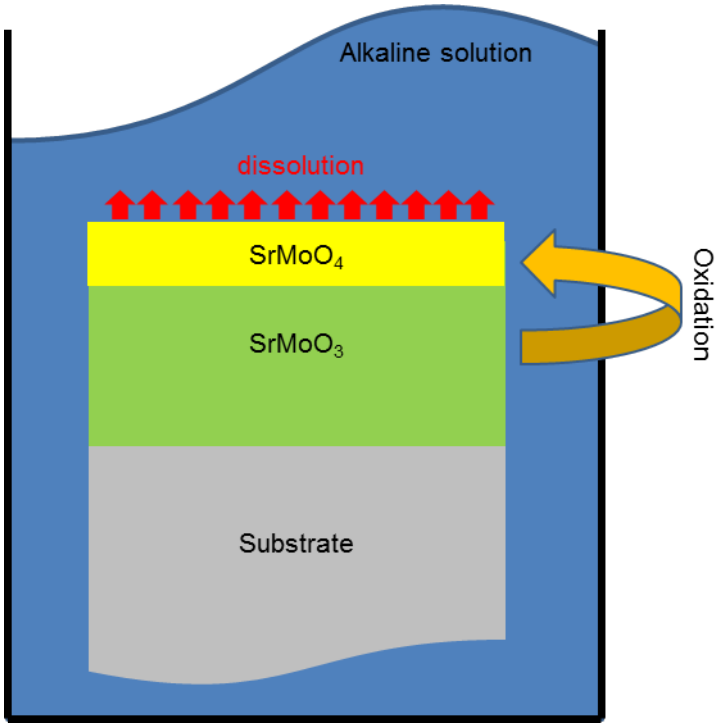

Fig. 3.4 Schematic of the proposed two-step etching mechanism of $SrMoO_3$: In the presence of oxygen, $SrMoO_3$ is oxidized (eq. 3.2) to $SrMoO_4$. The addition of H_2O_2 accelerates the oxidation process. At the second step (Eq. 3.3) the $SrMoO_4$ dissolves in the alkaline etchant.

The etching rate of SMO in the alkaline KOH solution as well as in the KOH-based AZ400 was tested. AZ400 is a conventional photoresist developer, available in many cleanroom facilities. Moreover, the effect of adding H_2O_2 on the etching rate of SMO was evaluated for both of the solutions. The alkalinity of all the tested etching solutions was constant (pH=14). The etching rate of the SMO in the tested etching solutions are presented in table 3.2.

The etching rate of the SMO by the KOH and AZ400 was less than a nanometer per second. This etching rate can be used to etch the SMO thin films with the moderate rate in a controllable manner. The additive H_2O_2 resulted in significant increase in the etching rate in both KOH and AZ400 solutions, confirming the mechanism explained in (3.1-3.3.)

The addition of the H_2O_2 had a stronger etching acceleration effect on the KOH solution. This is probably due to the reaction of the boric acid of the AZ400 with the H_2O_2 and production of

the peroxoborates. Thus, the effective concentration of the H_2O_2 in the AZ400 solution would be lower than that of the KOH solution with the same amount of additive H_2O_2.

Table 3.2 the etching rate of alkaline solutions with and without oxidizing agent (H_2O_2)

Etchant	*pH*	*Content*	*Etching Rate (nm/s)*
KOH	*14*	*KOH 4g+ 1 liter H_2O*	*0.6*
AZ400	*14*	*200 ml AZ400 + 800 ml H_2O*	*0.7*
KOH + H_2O_2	*14*	*50ml (KOH 4 g/l) + 0.1ml H_2O_2*	*14.5*
AZ400 + H_2O_2	*14*	*50ml (AZ400 1:4 H_2O) + 0.1ml H_2O_2*	*4*

One of the main implications of this study is that the rate-limiting step of the etching process of the SMO is the oxidation of Mo^{4+} to Mo^{6+}. Thus, it is possible to tailor the etching rate of the SMO in the alkaline solutions by choosing the right amount of oxidizing additives such as H_2O_2. Another significant finding of this study is that low concentrations of alkaline solutions can be used to remove the superficial $SrMoO_4$ from the $SrMoO_3$. Such a step results in ohmic contact with electrical probes with the SMO sample for the future studies and applications. Finally, a controllable and reliable method for wet chemical etching of the SMO was established. The knowledge acquired from this work can be used to pattern SMO thin films in the future in the fabrication of microelectronic devices.

3.3.2. Electrical conductivity of SMO at microwave frequencies

SMO samples were deposited on 5 x 5 mm (110) GSO substrates, as explained in the 3.3. The AZ400 solution, as described in 3.3.1, was used to pattern Coplanar Waveguide (CPW) structures by photolithography and wet chemical etching. Each CPW structure consisted of a signal line with a width of 25 µm and two grounds each 280 µm in width. A Dektak surface profiler was used to measure the lateral dimensions of the sample. Taking into account the

permittivity of GSO and the thickness of the SMO layer, the width of the signal stripe and the gap between the signal and ground stripes were modeled, aiming at a transmission line impedance of around 50Ω.

Each sample finally consisted of eight CPWs of SMO each 3mm in length. The overall structure of the CPWs and the contact pad of the signal stripe are shown in Fig. 3.5. Two ends of the same CPW structure were used for contacting to measure the reflection and transmission signals. To build a reference sample, 140nm thick Au film was electroplated on GSO substrate. Lift-off lithography was used to form the CPW structure. The central signal stripe was 20µm in width and 3 mm in length. Ground patches were 30 µm apart from the signal line. An Anritsu vector network analyzer 3739vc was used to measure the reflection and transmission signals. The network analyzer was calibrated using a standard calibration alumina kit with gold contacts using short-open-load-through (SLOT) test. The S_{11} and S_{21} (scattering reflection and transmission, respectively) were measured at microwave frequencies up to 20 GHz. To remove the thin isolating $SrMoO_4$ surface layer from the surface of the SMO CPWs before contacting, the sample was dipped in the AZ400 solution (see section 3.3.1) before the microwave resistivity measurements.

For extraction of the frequency dependence of resistivity, the insertion loss (S_{21}) of the Au and SMO CPWs were simulated. A commercial full-wave solver by Agilent was used to simulate the insertion loss of the Au by the method of moments (MoM). The geometry of the Au CPW structure, as well as the real component of the permittivity of the GSO substrate, was taken into account. By setting the $\tan\delta_{GSO} \approx 0.02$ and $\rho_{Au} \approx 3.9$ µΩ.cm at f =10GHz the best fit between the simulation and experimental curves were obtained (Fig. 3.6).

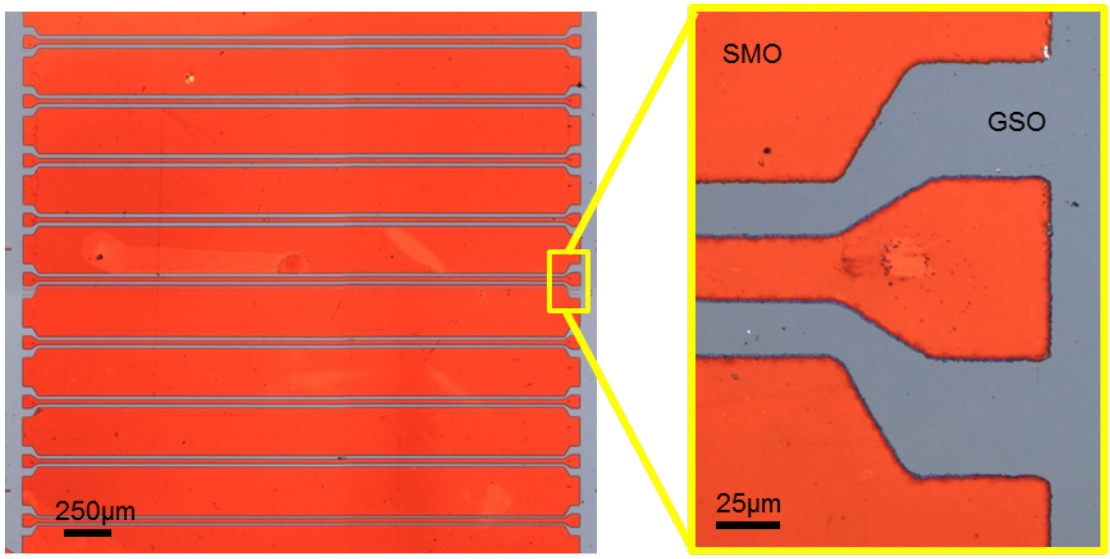

Fig 3.5 CPW structures of SMO thin film on the GSO substrate

The geometrical dimensions of the SMO CPWs and $\tan\delta_{GSO} \approx 0.02$ were used in the same manner to simulate the insertion loss of the SMO CPWs up to 20 GHz. The best fit was obtained by assuming a resistivity of $\rho_{SMO} \approx 29$ μΩ.cm at 10GHz. Deviations in the SMO measurement and simulation curves can be attributed to the lesser degree of fabrication precision of the SMO CPWs compared to the Au CPWs. This is because wet chemical etching results in less precise edge profiles as compared to the lift-off lithography, used for Au CPWs.

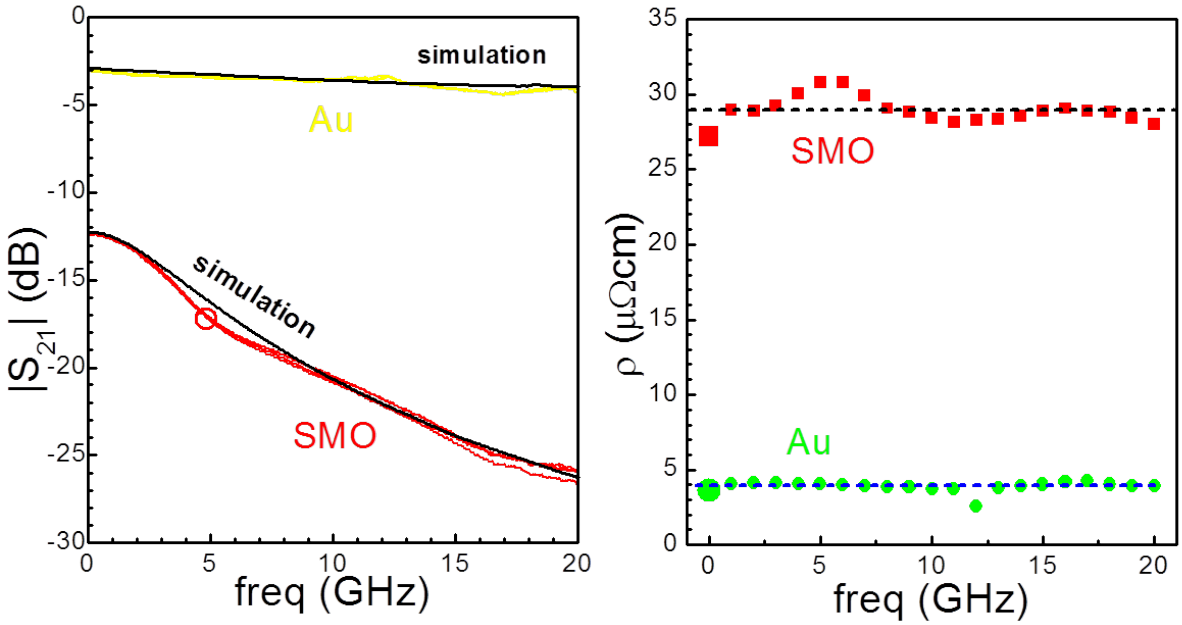

Fig. 3.6 (a) Frequency dependence of the insertion loss S_{21} for 4 Au (solid yellow lines) and 4 SMO (solid red lines) CPWs. The black curves show the simulated insertion loss of SMO and Au CPWs. (b) Frequency dependence of resistivity for SMO and Au extracted from the S_{21} simulations at each frequency point. Blue and black dashed lines show the average resistivity of Au and SMO, respectively.

In conclusion, highly epitaxial SMO with a smooth surface was fabricated. SMO thin films showed a consistently low resistivity of $\rho_{SMO} \approx 29$ μΩ.cm up to 20 GHz. Thus, SMO is an excellent electric conductor for integration into epitaxial heterostructures for microwave applications. Details of this study are to be found in [7].

3.4. STO capping

Deposition of the BST for fabrication of thin film varactors requires high temperatures (500-700 °C) and high oxygen pressures. Thus, the bottom electrode needs to withstand the temperature and oxygen atmosphere for BST thin film deposition. Therefore, the oxide resistance and temperature stability are known to be the core requirements for the bottom electrode[11]. SMO, on the other hand, is a meta-stable material, prone to oxidation. In the presence of oxygen, the $SrMoO_3$ changes to the $SrMoO_4$ and causes several problems. Firstly, the lattice structure of the $SrMoO_4$ does not match that of the BST and thus the BST will not grow epitaxially. Furthermore, the $SrMoO_4$ is an insulating material and therefore it is counted as a dead layer, degrading the electrical properties of such a stack at higher frequencies. Therefore, it is crucial to hinder the oxidation of the SMO, while keeping the epitaxial relation of the heterostructure for the deposition of the dielectric BST.

In this work, a thin layer of $SrTiO_3$ has been used as the capping layer to serve as a barrier for the oxygen and also to keep the lattice relation to the underlying SMO layer. STO provides a stable oxidation potential gradient and thus facilitates the interfacial transition between a reduced meta-stable conductor (SMO) and an oxidized insulator. STO provides a stable oxidation potential gradient and thus facilitates the interfacial transition between a reduced meta-stable conductor (SMO) and an oxidized insulator. Details of the interface engineering of this layer will be published elsewhere.

KrF excimer laser at 248nm wavelength was used to ablate a dense $SrTiO_3$ target material. A fluence of 1.5 J/cm^2 and laser repetition rate of 2Hz in ultrahigh vacuum (UHV, 10^{-8} Torr) were used to deposit a thin layer (4 nm) of STO on the SMO. The deposition of the STO capping layer was monitored by the *in situ* RHEED. As it can be seen in the STEM image of the cross section of the sample (Fig. 3.7, left), the excellent crystal quality of epitaxial STO on the SMO was achieved. Moreover, the layer-by-layer growth of the STO on the SMO is confirmed by the RHEED image of the surface of the STO capping layer (Fig. 3.7 top-right).

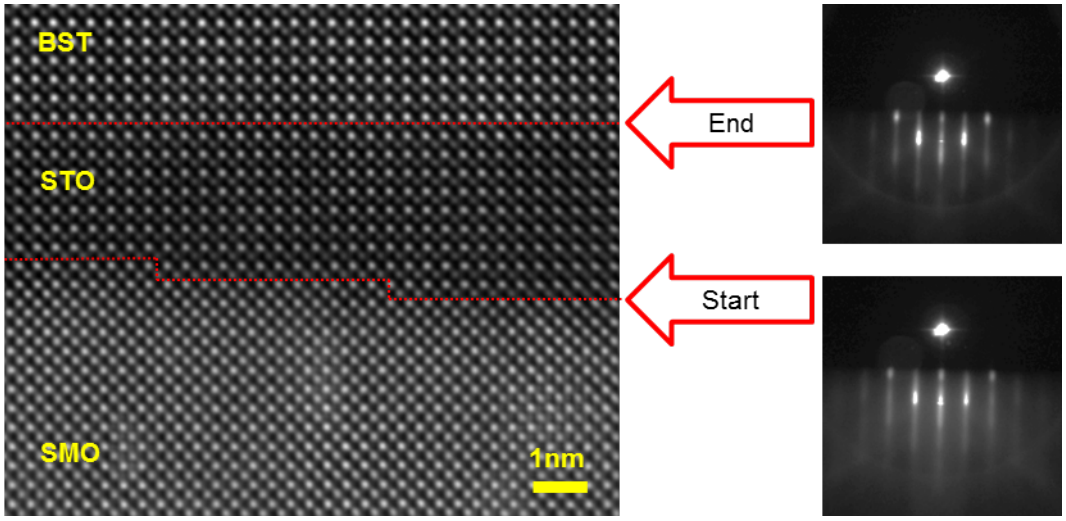

Fig. 3.7 STEM image of the SMO/STO interface. The *RHEED* images before and after the deposition of 8-10 monolayers of STO are shown in the right panels.

At the elevated temperature of 600 °C, the STO capping layer is capable of hindering the oxidation of the SMO layer at oxygen pressures up to 8 mTorr. It was observed that higher oxygen pressures or temperatures result in an immediate change of the RHEED pattern to a spotty reflection, suggesting the oxidation of the surface of the SMO, and thus, change of the reflection pattern of the STO layer accordingly. Further details on the interface engineering of SMO will be published elsewhere.

3.5. BST deposition

In this section, the deposition optimization of $Ba_{0.6}Sr_{0.4}TiO_3$ using PLD is presented.

In this study, a dense pallet of $Ba_{0.6}Sr_{0.4}TiO_3$ was used as the target material in the PLD process. The goal of this study was to optimize the deposition conditions and growth parameters of the BST on GSO for various background oxygen pressures, bearing in mind that the growth of the BST on top of the SMO will require precise tuning of the oxygen content in the deposition chamber.

As a starting point a temperature of 700 °C, a background pressure of 10mTorr, laser repetition rate of 4Hz, and a laser spot size of 2.5 mm^2 were used. The effect of laser fluence on the quality and out-of-plane lattice constant of the BST films was evaluated. Six BST films at different laser fluences, ranging from 0.3 J/cm^2 to 1.5 J/cm^2 were deposited. The out-of-plane θ–2θ X-ray diffraction patterns near the (002) reflection of the BST films are shown in Figures 3.8. The star denotes the (220) reflection of the $GdScO_3$ substrate. For all the used

fluences, the BST films showed a good degree of epitaxy. The film deposited by 0.5 J/cm^2 of fluence shows an out-of-plane lattice constant of 3.97, only 0.3% different from that of the bulk $Ba_{0.6}Sr_{0.4}TiO_3$. Furthermore, the pronounced Laue oscillations indicate excellent crystal quality and homogeneously grown BST films. Thus, this value is taken as the optimum fluence value at the used deposition conditions. Fig. 3.8 also suggests that the fluence can widely be used to tailor the stoichiometry of the BST film.

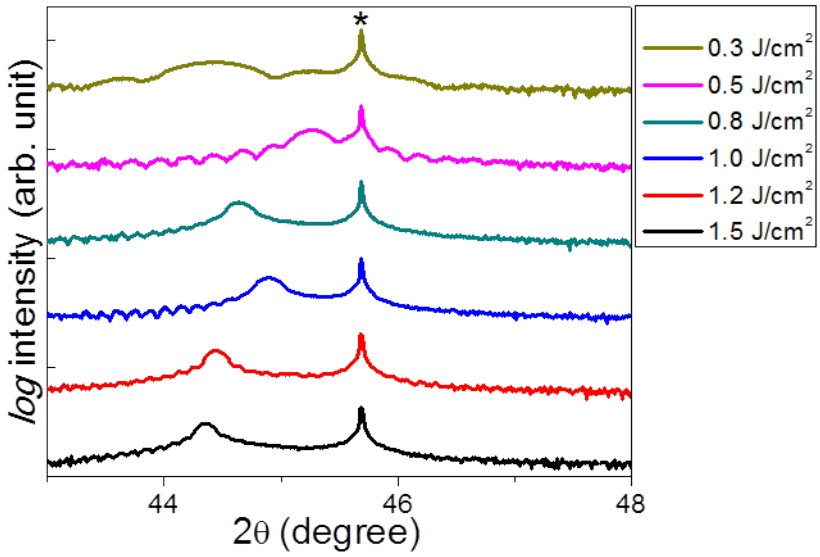

Fig. 3.8. The out-of-plane θ–2θ X-ray diffraction patterns near the (002) reflection of the BST films deposited at different laser fluences. The star sign denotes the (220) reflection of the $GdScO_3$ substrate

In the second step, the influence of substrate temperature on the BST film quality was studied. A laser fluence of 0.5 J/cm^2 was taken from the fluence optimization study. A background pressure of 10 mTorr, laser spot size of 2.5 mm^2, laser repetition rate of 4Hz were used.

As it can be seen in Fig. 3.9, the film deposited at a substrate temperature of 700 °C shows the closest out-of-plane lattice constant to that of the bulk value, suggesting the best stoichiometric match to the desired Ba/Sr=3/2.

It can also be seen that a minute change in temperature by 20 °C results in a shift of the peak to the right, which is an indicator of the shrinkage of the out-of-plane lattice component. This could be due to lesser Ba content. At the elevated temperature of 750 °C, the reflection becomes very broad, exhibiting non-uniformity of the lattice structure. Nevertheless, the sample is still epitaxial. At 650°C, the out-of-plane lattice component shows a strong shift to

the right, suggesting extra Ba content in the film. Among the tested substrate temperatures, 700 °C is the optimal temperature.

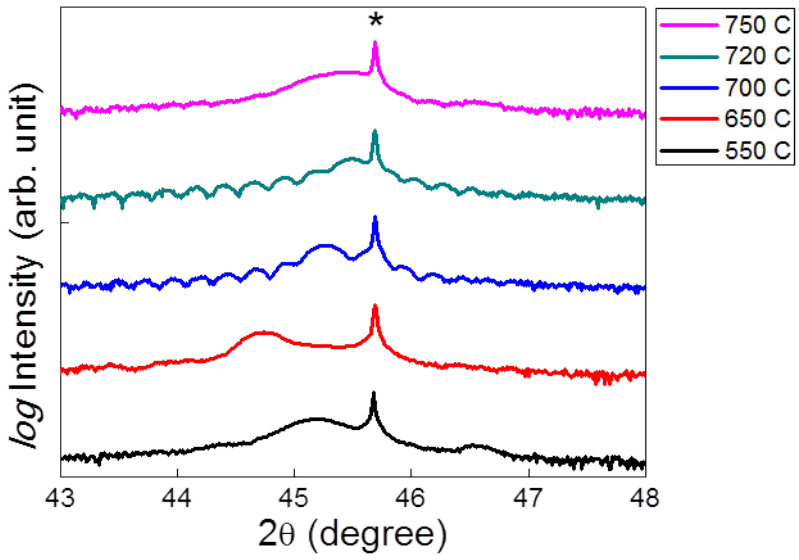

Fig. 3.9. The out-of-plane θ–2θ X-ray diffraction patterns near the (002) reflection of the BST films deposited at different Temperatures. The star sign denotes the (220) reflection of the $GdScO_3$ substrate.

After having acquired the optimal parameters for deposition of BST at ten mTorr oxygen pressure, it was necessary to fine-tune the deposition parameters at slightly lower oxygen pressures to be able to use these deposition conditions for fabrication of the varactors based on SMO bottom electrodes.

It was observed that by keeping other deposition parameters constant, it is possible to tune the quality of the deposited film at various pressures through tailoring the laser fluence. In fig. 3.10, it can be seen that at 1mTorr of oxygen pressure, by lowering the fluence, an epitaxial BST with a reasonable out-of-plane lattice constant (peak position) and uniformity (symmetric and pronounced Laue oscillations) can be obtained. The oxygen in the chamber, not only chemically interacts with the species in the plume and on the surface of the substrate, but also serves as a physical barrier for the ablated materials moving towards the substrate. Thus, the higher the background pressure, the lesser the mean free path of the ablated species. Thus, for lower oxygen pressures lower fluences should be used and vice-a-versa. This is in agreement with the observation in the Fig. 3.10 that deposition at lower background pressures required also lower fluence.

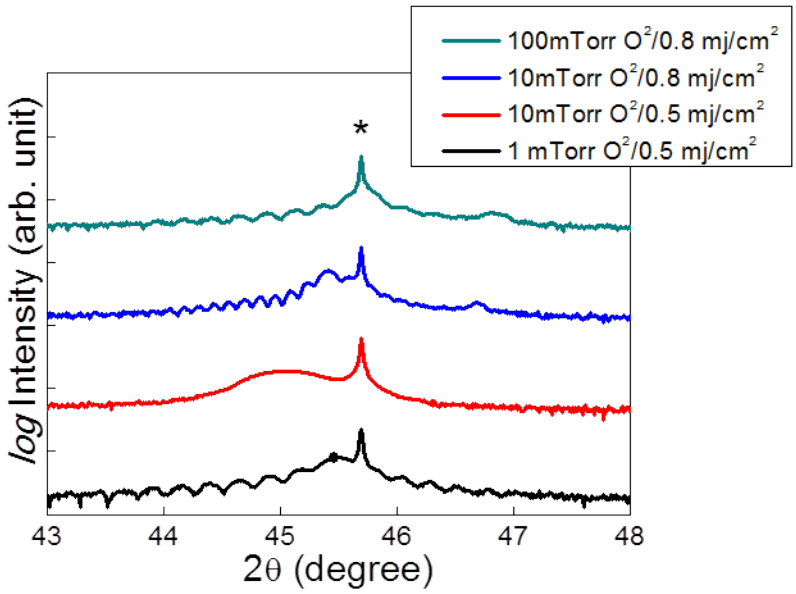

Fig. 3.10. The out-of-plane θ–2θ X-ray diffraction patterns near the (002) reflection of the BST films deposited at different fluences and oxygen pressures. The star sign denotes the (220) reflection of the $GdScO_3$ substrate.

In conclusion, a laser fluence of 0.5 J/cm^{2,} background pressure of 1 mTorr, laser spot size of 2.5 mm^2, and a laser repetition rate of 4Hz were chosen as the optimal PLD parameters for deposition of the BST on top of the STO-capped SMO.

3.6. Top electrode deposition

Lift-off lithography was used for the realization of top electrodes with the desired configuration on the varactors. The top electrodes consisted of a thin layer (~20nm) of Platinum and a thicker layer (~350nm) of gold. In this section, the optimization of lift-off process is explained.

The photolithographic mask was designed in a way that 36 varactors would be measurable in each sample, independently. To be able to extract more data from measurement of each sample, top contacts with different sizes were used. However, to check the uniformity and reproducibility of data on different parts of the sample, the 36 varactors were grouped in 4 similar blocks, each containing nine varactors. In each block, four varactors had the smallest feature sizes (d=20 µm, D=40 µm). Furthermore, by varying the diameter of the signal pad (d) and the gap (D-d), it was possible to extract the BST loss tangent and also to reconfirm the influence of the top electrode size on the total quality factor. Fig. 3.11 shows the schematic of the top electrode configuration on a substrate (top left) and the dimensions of a

single varactor (top right). Table 3.3 provides the dimensions of each of the 36 varactors, patterned on each sample.

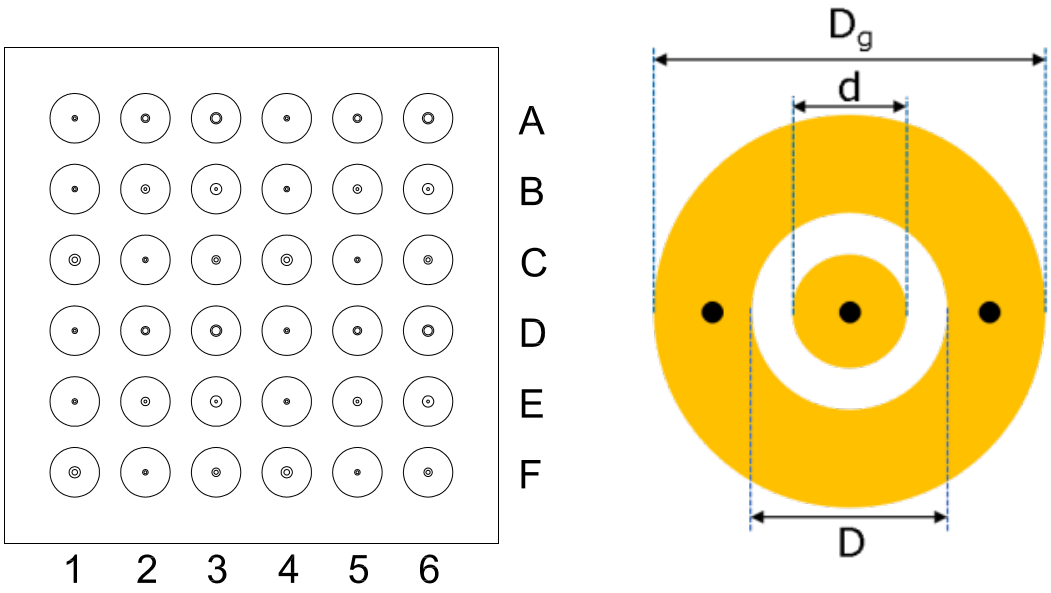

Fig. 3.11 Schematic of the top electrode configuration on a 5x5 mm substrate (top left), and the dimensions of each single varactor (top right).

Table 3.4 Dimensions of each of the pads in Fig. 3.11.

column / *Row*	*1 & 4*		*2 & 5*		*3 & 6*	
	d (µm)	*D (µm)*	*d (µm)*	*D (µm)*	*d (µm)*	*D (µm)*
A & D	*20*	*40*	*40*	*60*	*60*	*80*
B & E	*20*	*40*	*20*	*60*	*20*	*80*
C & F	*40*	*80*	*20*	*40*	*30*	*60*

In conclusion, the deposition, processing, and fabrication of varactor test structures were optimized. In the next section, fabrication and characterization of the state-of-the-art thin film BST varactor based on SMO bottom electrode will be explained.

4. All-oxide varactor with $SrMoO_3$ bottom electrode

In this section, microstructural properties and electrical performance of the State-of-the-art $Ba_{0.4}Sr_{0.6}TiO_3$ varactors using highly conducting $SrMoO_3$ as bottom electrode will be presented.

4.1. Sample fabrication

Single crystalline $GdScO_3$ (GSO) in (110) orientation was used as substrate material. A surface area of 5x5 mm^2 provided enough space for fabrication of 36 parallel-plate varactors (MIM structure) which could be measured and characterized independently (for details see: section 3.6). The substrate surface was blown by nitrogen before insertion in the PLD chamber. No further surface cleaning and treatment was performed. The GSO has an Orthorhombic structure (lattice parameters a=5.482A, b=5.742A, and c=7.926A) with a pseudocubic lattice parameter of 3.967A, providing a low lattice mismatch for epitaxial growth of the SMO and $Ba_{0.4}Sr_{0.6}TiO_3$. Pulsed Laser Deposition (PLD) with a KrF excimer laser (λ=248nm, T=30ns) was used to deposit the STO/SMO/STO/BST on the GSO substrate. The initial STO buffer layer of 5 unit cells was deposited on the GSO substrate to enhance the initial growth of SMO. The SMO layer (320nm) was deposited consecutively, followed by the deposition of 10-mono-layers of STO and 83 nm of BST. The deposition conditions, as well as the thicknesses of each layer, are listed in Table 4.1. The thickness of the $SrTiO_3$ layers was calculated using RHEED intensity oscillations. The thickness of BST and SMO were measured from the thickness fringes of the *2θ-θ* scan.

Table 4.1. PLD deposition parameters and thickness of each layer of the varactor heterostructure.

Sequence	*Material*	*Number of pulses*	*Laser repetition rate (Hz)*	*Pressure (Torr)*	*Laser energy density (j/cm^2)*	*Thickness (nm)*
1	*$SrTiO_3$*	*100*	*2*	*1E-8*	*0.5*	*2*
2	*$SrMoO_3$*	*16000*	*5*	*1E-8*	*0.5*	*320*
3	*$SrTiO_3$*	*200*	*2*	*1E-8*	*0.5*	*4*
4	*$Ba_{0.4}Sr_{0.6}Ti0_3$*	*4000*	*4*	*1E-3 (O_2)*	*0.5*	*83*

To deposit the top electrodes on the sample, a single lift-off step was employed. The parameters used for achieving a 6-µm-thick photoresist are listed in Table 4.2. The edge profile of the photoresist exhibited slight undercut which assisted the lift-off process.

Table 4.2. Photolithography parameters for lift-off patterning of Pt/Au.

Resist	*Spin coating speed /duration (s)*	*Pre-bake Temp.°C /duration (s)*	*Exposure duration (s)*	*Development agent/duration (s)*	*Post exposure duration (s)*	*O_2 Plasma etching duration (s)*
maN490	*5000rpm/60*	*90°C/240s*	*150*	*maD332s:H2O (1:4)/135*	*200*	*60*

Top electrodes with varying dimensions (See section 3.6) were deposited through the lithographic mask using room temperature magnetron sputtering. The sputtering parameters for deposition of Platinum and Gold and the final thicknesses of theses layers, measured by stylus profilometry are listed in Table 4.3.

Table 4.3. Sputtering parameters for deposition of top electrodes and the thickness of the deposited layers.

Material	*sputtering pressure (Torr)*	*Current (mA)*	*Duration (s)*	*deposition rate (nm/s)*	*Final Thickness (nm)*
Platinum	*10^{-4}*	*30*	*80*	*0.25*	*20*
Gold	*10^{-4}*	*50*	*500*	*0.70*	*350*

After deposition of the top electrodes, the sample was soaked in acetone for one hour. Due to optimized lift-off procedure and undercut of the photoresist, the photoresist was easily lifted off with a slight agitation of the solution (Fig. 4.1). This resulted in a clean sample surface with well-defined electrode structures. The schematic of the final structure and the corresponding thicknesses are presented in Fig. 4.2.

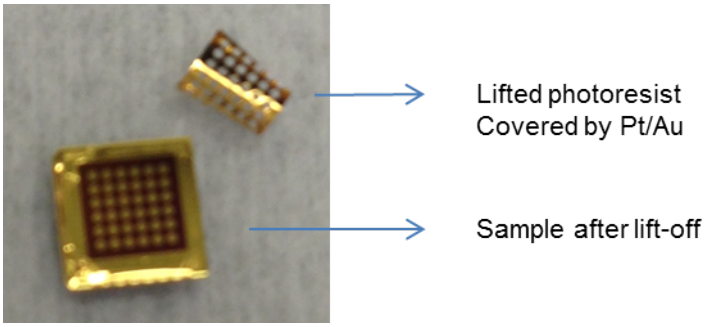

Fig. 4.1 Image of the sample inside the Acetone after the lift-off process. The rolled foil is the lifted photoresist which is covered by 20 nm of platinum and 350 nm of gold.

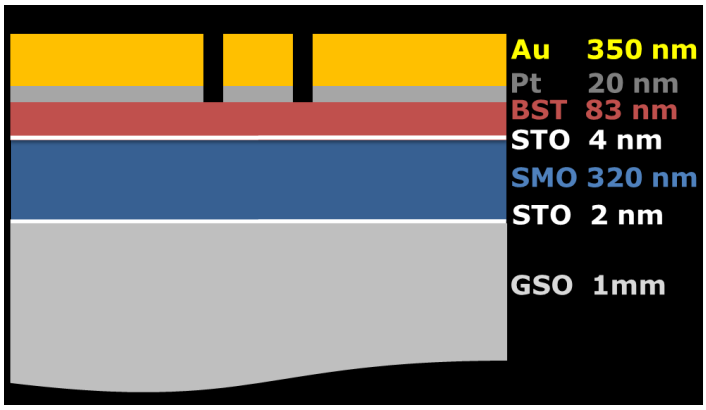

4.2. The schematic of the final structure and the corresponding thicknesses.

4.2. Microstructural analysis

Three methods were used to monitor and evaluate the microstructural properties and crystallinity of the $GdScO_3/SrTiO_3/SrMoO_3/SrTiO_3/Ba_{0.4}Sr_{0.6}TiO_3/Pt/Au$ heterostructure during and after the deposition: *in situ* monitoring of growth by RHEED (only for deposition of oxide layers), X-Ray diffraction analysis including residual stress mapping, and scanning transmission electron microscopy (STEM). In the following sections, results of these analysis will be presented.

4.2.1. RHEED

The RHEED *in situ* monitoring was used during the growth of the oxide layers in the PLD deposition chamber. Fig. 4.3 shows the RHEED pattern of the surface of the sample before the

deposition of each layer. For the first STO layer and the beginning few layers of the SMO, clear intensity oscillations were observed in the RHEED pattern (See section 3.2), suggesting a layer-by-layer growth. However, the rest of the SMO growth, as well as the capping STO and the BST layer, did not show a strong RHEED intensity oscillation, yet a streaky RHEED pattern, suggesting a step-flow growth.

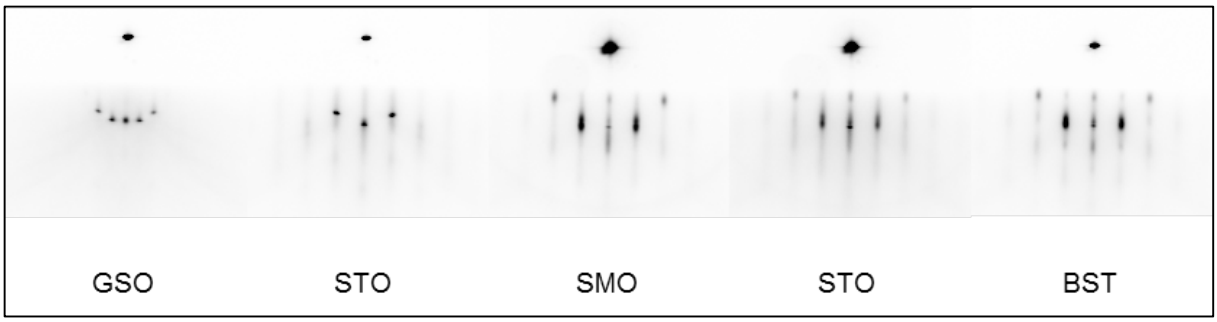

Fig. 4.3. RHEED patterns of the surface of each layer before deposition of the next layer.

4.2.2. X-Ray diffraction

After the completion of the deposition of the $SrTiO_3/SrMoO_3/SrTiO_3/Ba_{0.4}Sr_{0.6}TiO_3$/Pt/Au on the $GdScO_3$, the X-Ray diffraction of the sample was measured e*x-situ*. The coupled scan (*2θ-θ*) suggests a single-phase heterostructure (Fig. 4.4). No reflections from the Pt and thin STO layers are observable. The unidentified peak at 2θ=67.8 is an occasional unknown peak which has been observed for SMO on GSO. Moreover, the presence of symmetric Laue oscillations near the (002) BST and SMO peaks (Fig 4.5) exhibits highly coherent and homogeneous growth. The STO buffer and capping layers are too thin for having a pronounced reflection peak which most probably would be masked by the background of the BST peak in the *2θ-θ* spectrum.

The out of plane lattice parameters of the SMO and BST films were calculated using Nelson-Riley equation. Moreover, the exact position of the Laue fringes close to the (002) SMO and (220) GSO were used to derive the thickness of the STO and SMO layers (Fig. 4.5). Results of these calculations are listed in Table 4.4.

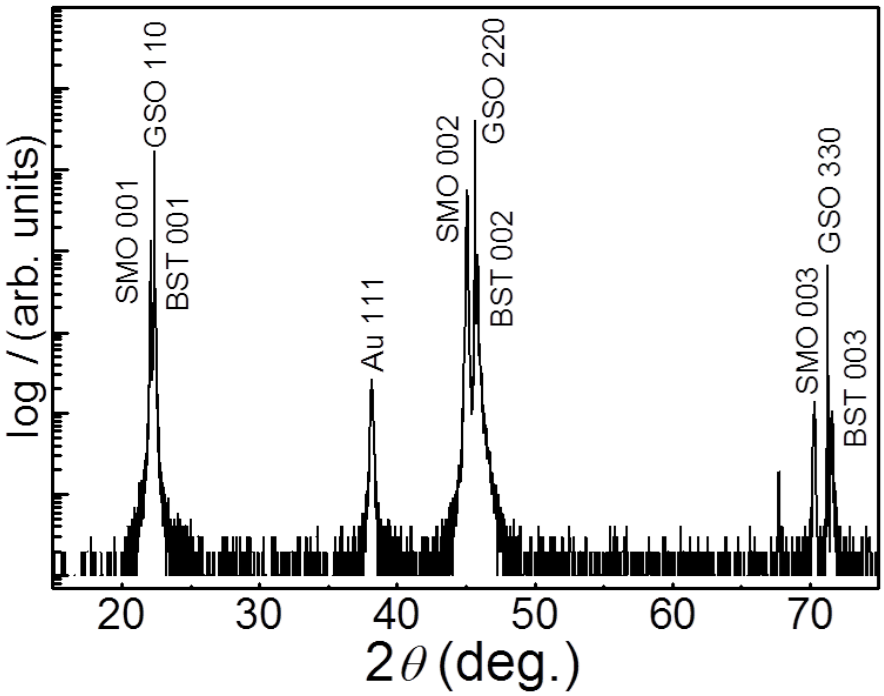

Fig. 4.4. The X-ray diffraction θ–2θ scan of the GSO/STO/SMO/STO/BST/Pt/Au heterostructure.

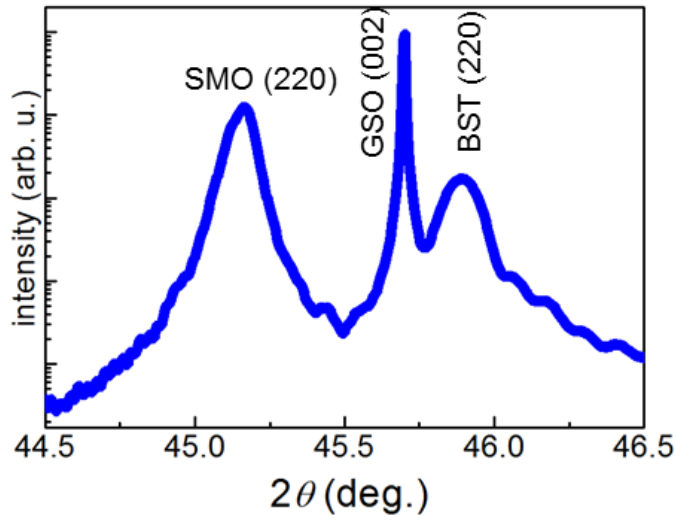

Fig. 4.5. The X-ray diffraction θ–2θ scan of the GSO/STO/SMO/STO/BST/Pt/Au heterostructure near the (002) GSO peak.

Table 4.4. Peak angle (2θ) and respective thickness and out-of-plane lattice constant values, calculated using the X-Ray diffraction 2θ-θ spectrum close to the (220) SMO and (220) BST peaks (Fig. 4.5).

Reflection	*peak angle (θ)*	*c-lattice (nm)*	*c-lattice bulk value (nm)*	*Thickness (nm)*
GSO (220)	*45.7012*	*0.39641*	*0.3967*	-
$Ba_{0.4}Sr_{0.6}Ti0_3$ (002)	*45.8919*	*0.3952*	*0,3940*	*84*
SMO (002)	*45.1551*	*0.40105*	*0.3975*	*307*

To check the mosaicity and the uniformity of the crystal structure across the thickness, rocking curve measurements (ω-scan) close to the (002) SMO were performed (Fig. 4.6). The full width at half maximum (FWHM) of the rocking curve of SMO and BST are 0.035 and 0.05, respectively.

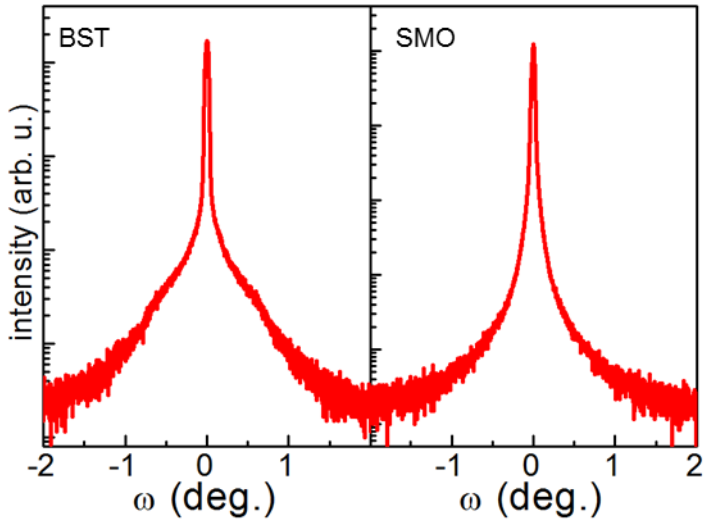

Fig. 4.6. Rocking curve (ω-scan) of the SMO close to the (002) peak

The low diffusive background of ω-scan profiles of the SMO and BST suggest low defect densities in both layers.

To evaluate the in-plane lattice correlation between the substrate and the deposited SMO and BST layers, X-ray diffraction residual stress mapping was performed. As it can be seen in Fig. 4.7, the peak intensities of the (420) GSO, 013 (BST), and 013 (SMO) reflections are aligned along the $Q_{\perp}$ axis, suggesting that the in-plane lattice of the SMO and BST are commensurately strained and locked to the in-plane lattice of the GSO substrate.

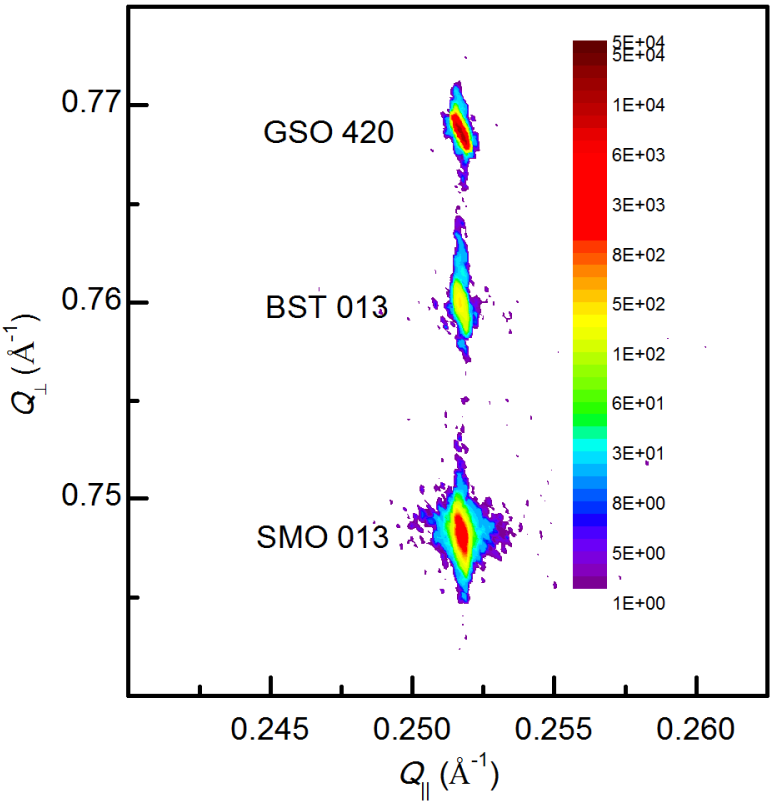

Fig. 4.7. Residual Stress Map (RSM) of the (420) GSO, (013) BST and (013) SMO planes.

This implies the following relation between the crystal planes of the GSO substrate, and SMO and BST layers: GSO[110] || SMO[001] || BST[001].

Therefore, the in-plane lattice parameters of BST and SMO are equal to the pseudocubic lattice parameter of GSO ($a=b=0.39641$). Thus, by using the bulk lattice parameter of 0.3940 for the $Ba_{0.4}Sr_{0.6}Ti0_3$ (Table 4.4), the tensile strain in the BST film will be 0.8%. Similarly, taken into account the bulk lattice parameter of 0.3975 for SMO (Table 4.4), the SMO is compressional strained by 0.2%.

4.2.3. High-Angle annular dark-field (HAADF) scanning transmission electron microscopy (STEM)

The FIB sample preparation and the STEM study were done by Dr. L. Molina-Luna and Dr. J. Verbeeck at EMAT, University of Antwerp, Belgium.

Focused Ion Beam (FIB) was used to cut a lamella of the GSO/STO/SMO/STO/BST/Pt/Au heterostructure. The cross section of the lamella was used to take (HADDF) STEM image from the full stack of the heterostructure.

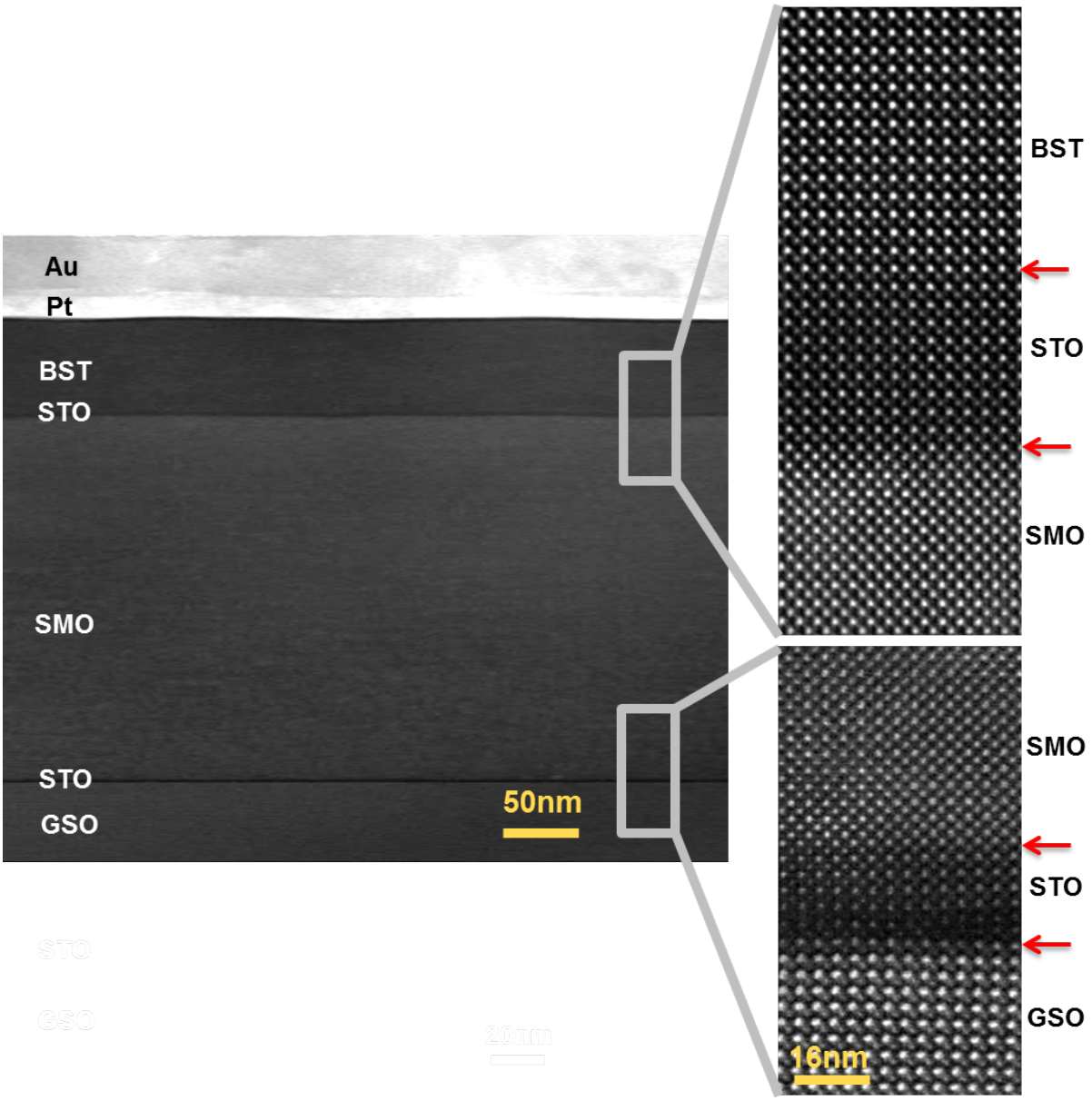

Fig. 4.8 HADDF-STEM image of the cross section of the GSO/STO/SMO/STO/BST/Pt/Au lamella.

Fig. 4.8 shows the (HADDF) STEM image of the cross section of the heterostructure. The image confirms the relative thicknesses of SMO and BST measured by XRD, and Platinum and Gold measured by stylus profilometer (Table 4.1 and 4.3). Moreover, the sharp interfaces at the overview STEM image (left panel) confirm the excellent growth of layers with smooth surfaces. Misfit dislocations nucleate during the growth of the STO layer on the GSO, visible in the bottom right image (Fig. 4.8). These dislocations not only help to relieve the misfit strain but also most likely accommodate the excess energy of the ScO_6 octahedra in the orthorhombic GSO. In the bottom right image of fig 4.8, a lattice tilt of 3° between the GSO and STO is clearly seen.

In contrary to the STO/GSO interface, the rest of the oxide interfaces in the heterostructure (STO/SMO/STO/BST) possess cubic perovskite structure with A^{2+} - B^{4+} valences. Thus, these interfaces are sharp with no observable dislocation or tilt, as it can also be seen in Fig 4.8 (top right panel).

4.3. Electric properties at microwave frequencies

Dielectric properties of the sample were measured over a frequency range of 100 MHz to 20 GHz using an Anritsu 37397c impedance analyzer and a Keysight Technologies VNA vector network analyzer. A standard calibration kit with short-open-load-thru (SLOT) structures on alumina was employed to measure the reflection coefficient S_{11} of the test structure. Ground-Signal-Ground (GSG) on-wafer probes with 150 µm pitch were used to contact the test structure. In this section, results of this measurement will be presented.

The Voltage dependence of the electric permittivity ε_r and capacitance C at 1 GHz are shown in Fig. 4.9. The obtained C(V) curve with $C(0) \approx 5$ pF is in the range of reported values for the MIM varactors with platinum bottom electrode[81]. As expected for thin films, the $\varepsilon_r \approx 180$ is lower than $\varepsilon_r \approx 1000$ reported for $Ba_{0.4}Sr_{0.6}TiO_3$ single crystals. As mentioned in section 1.4, the Curie temperature of BST thin films is typically shifted as compared to the bulk. The BST layer ($x = 0.4$) of the varactor at room temperature could be within or near the ferroelectric phase transition.

In order to investigate the weak hysteresis in the ε(V) in Fig. 4.9 and also to identify the source of the hysteresis curve, the sample was heated up to 80 °C. Fig. 4.10 is a comparison of the permittivity curve of the same sample under the same bias at room temperature and 80 °C.

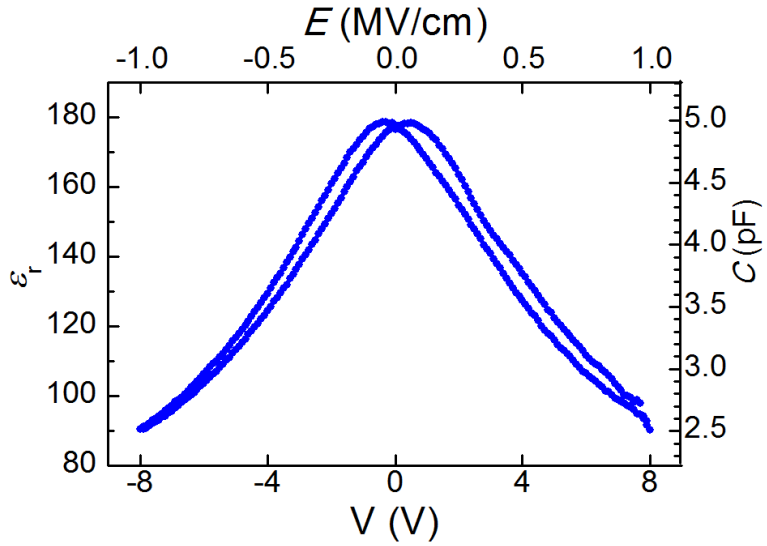

Fig. 4.9 Voltage (Electric Field) dependence of permittivity and capacitance C at 1 GHz.

As it can be seen in Fig. 4.10, at an elevated temperature of 80 °C, which should be far above the Curie temperature, the hysteresis effect persists. At temperatures above the Curie temperature, the remnant polarization curve can be due to strain-induced residual ferroelectric domains or local polar regions, due to defects such as oxygen vacancies. The BST film in this study is grown at a low oxygen pressure of ~ 1 mTorr to prevent undesired oxidation of the underlying SMO layer. Thus, it is highly likely that the BST film grown at such low oxygen pressure would have ample oxygen vacancies, resulting in local polar regions.

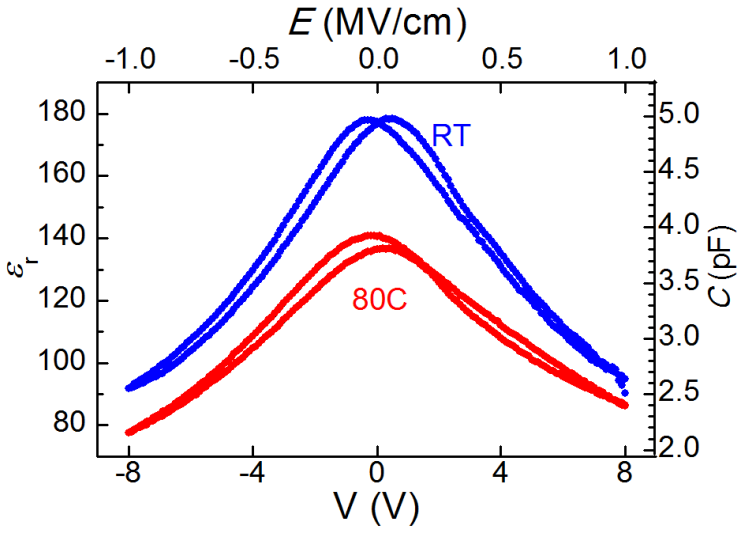

Fig. 4.10 Voltage (Electric Field) dependence of permittivity and capacitance C at 1 GHz at different temperatures.

The dielectric tunability of $n_r = 50\%$ is observed at 8 V (1 MV/cm) at 1 GHz (Fig. 4.11). Similar values are typically obtained at bias voltages higher than 20 V for the MIM (parallel-plate) varactors with Pt bottom electrodes and BST layers thicker than 300 nm[81]. The growth of the BST films thinner than 300 nm on Pt usually leads to electric short-circuits in the Pt/BST/Pt varactors due to the formation of hillocks in the Pt layers [11]. However, because the varactor in this study has much smoother and thinner dielectric layer (BST: 83nm), a comparably low voltage (8V) translates into a high electric field (1MV/cm). This value is among the lowest voltages reported so far for tuning a ferroelectric varactor up to $n_r = 50\%$.

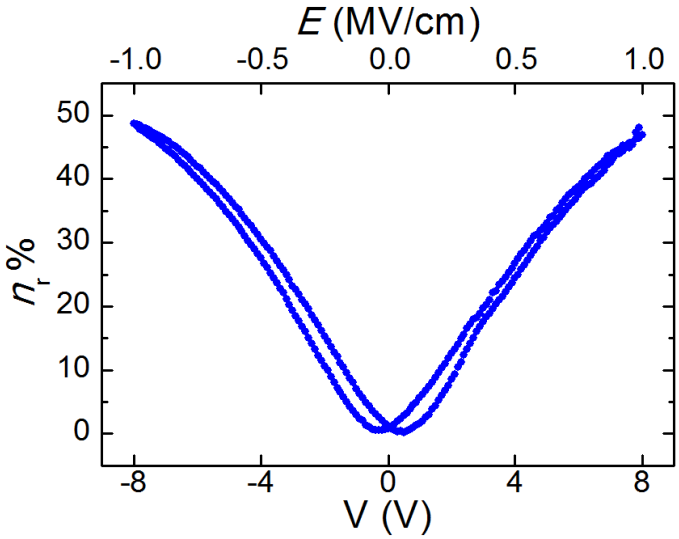

Fig. 4.11 Voltage (Electric Field) dependency of relative tunability n_r at 1 GHz.

The frequency dependence of the quality factor Q under no bias (0V) and at 8V are shown in Fig 4.12. An increase of quality factor with voltage is most likely related to the extrinsic loss (i.e. charged defects) mechanisms of the dielectric BST layer. The cross-over of the quality factor curve at 8V with the quality factor curve at 0V is due to the acoustic resonance under applied DC voltage.

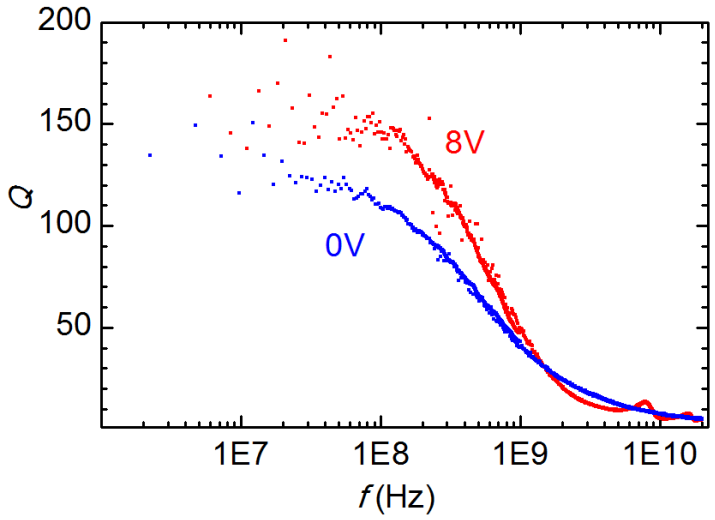

Fig. 4.12 Frequency dependence of quality factor *Q* at room temperature under 0V and 8V bias.

It has been shown that at lower microwave frequencies (KHz-MHz) total losses of the varactor are dominated by the dielectric loss[21]. However, at higher frequencies, the total loss tangent of the varactor ($1/Q_{tot}$) is dominated by the losses of the conductors[11]. Thus, the quality factor at GHz frequencies cannot be a decisive element in determining the quality of the dielectric material. Moreover, the geometrical factors such as shape and size of the top and bottom conductors have a large influence on the absolute value of the total varactor loss at upper MHz and GHz frequencies.

While materials scientists are interested in the quality of the dielectric layer, device engineers would like to see the pragmatic potential of the certain combination of materials for integration into devices. Thus, the total quality factor of an SMO-based MIM varactor test structure serves as a measure to show the potential of the SMO-based thin film varactors for low-voltage tunable components for microwave frequencies. In this context, the quality factor of 40 at 1 GHz is one order of magnitude better than the best oxide varactors reported so far [21].

There is always a trade-off between the quality factor and the tunability of thin film varactors[35]. Therefore, for device engineers, it is crucial to compare different varactors by a measure which would include both tunability and quality factor. Thus, the commutation quality factor (CQF) (Eq. 1.8) is commonly employed to compare the performances of the varactors in various studies. Fig. 4.13 shows the frequency dependence of the CQF in comparison to the CQF of the $SrRuO_3/Ba_{0.25}Sr_{0.75}TiO_3/Pt/Au$ varactors reported by Gevorgian

et al. [21]. As it can be seen, the CQF of the SMO-based varactor is almost two orders of magnitude higher than previously reported values for the best oxide-based varactor so far.

For industrial applications, a varactor needs to have a minimum CQF of 2000 [16], [21]. Thus, with current configuration and performance, the SMO-based varactors can be implemented up to 1 GHz. This result is already far better than what other groups have achieved using oxide electrodes in ferroelectric thinfilm varactors and suggests the high potential of SMO-based varactor technology.

To evaluate the dielectric performance of the BST layer, it is crucial to separate the dielectric loss tangent from the other contributing factors. Particularly in the GHz frequencies, the losses of the conducting oxide layer are known to be dominant and thus the total measured loss tangent of the test device is not the right gauge for judging the dielectric loss of the BST layer.

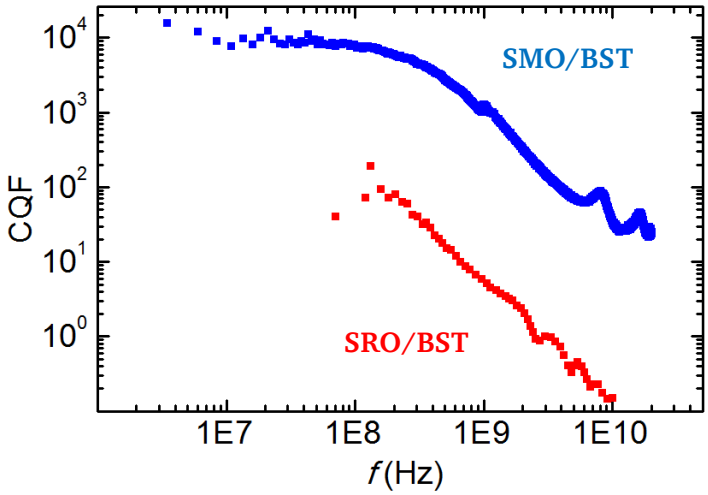

Fig. 4.13 Frequency dependence of CQF at room temperature for the sample of this study (SMO/BST) under 8V of bias, compared to the literature value for SRO/BST varactor under 10V of bias [21].

In this work, a lumped element approach was employed to model the equivalent circuit of the test structure. Using Advanced Design System (ADS) software, the influence of the series resistance of SMO was separated. Furthermore, the reflection coefficient of the *S*-parameter measurement was simulated by the frequency-domain method of moments (MoM). The simulation and modeling were done by M.Sc. Mohammad Nikfalazar at the IMP Institute of the Technical University of Darmstadt. The measurement results were fitted to the modeling of the equivalent circuit as well as to the MoM simulation curves. Fig. 4.14 shows a schematic

of the test structure and its corresponding equivalent circuit. It has been demonstrated that at higher frequencies (10 GHz) the parasitic capacitance between the top contact structures and also the parallel Resistor/Capacitor in the substrate are negligible [48]. Furthermore, when two capacitors with a significant difference in capacitance are connected in series, the smaller capacitance dominates the total capacitance, following equation 4.1:

$$\frac{1}{C_{tot}} = \frac{1}{C_1} + \frac{1}{C_2} \qquad 4.1$$

If $C_1 >> C_2$, then $C_{tot} = C_2$.

Considering that the area of the ground pad in the test structure is almost 400 times bigger than that of the signal pad, the capacitance of the ground pad is then negligible. Therefore, using a lumped approach, the equivalent circuit can be simplified as depicted in Fig. 4.14 (bottom), where R_{ser} is the series resistance of the SMO top electrodes, and contact resistances, L_{con} is the parasitic inductance of the conductor, and C_s is the capacitance of the dielectric BST with an area equal to that of the signal pad and 83 nm of thickness. The R_{BST} represents the fringing capacitances, the electrical length inductance, and the measurement tolerances.

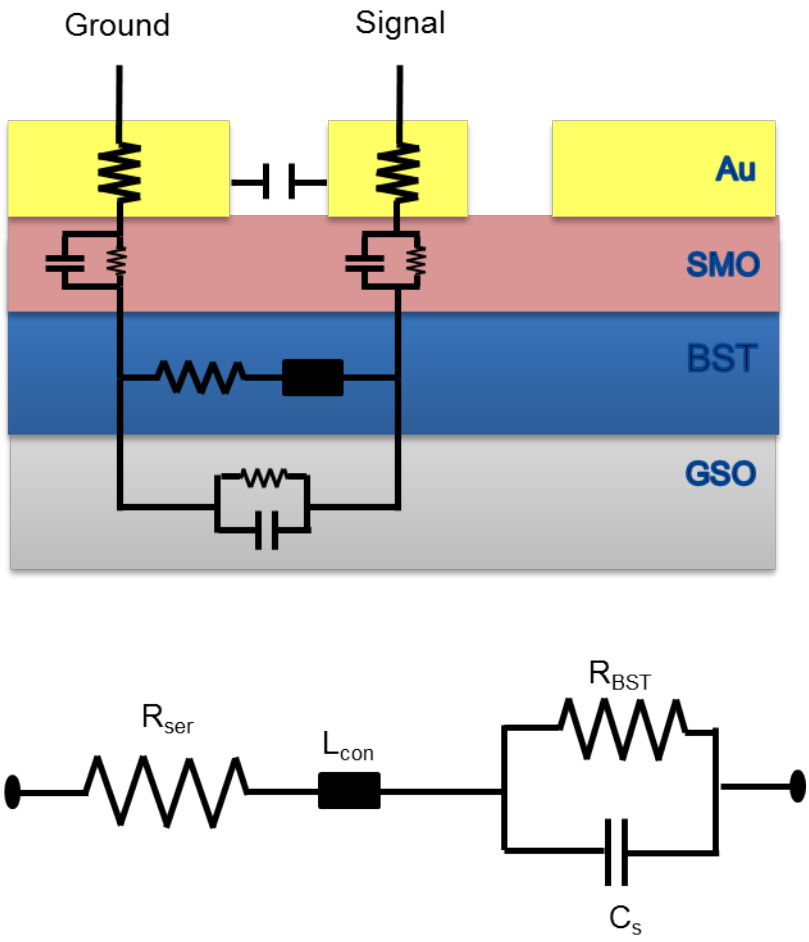

Fig. 4.14 Schematic cross section of the test structure (top) and its corresponding lumped equivalent circuit with parallel $R_P | C_P$ (bottom).

Based on the simplified equivalent circuit, the total losses of the test structure follow:

$$Z_{tot} = R_{ser} + j\omega L_{con} + \frac{R_{BST}}{1 + Q_\varepsilon{}^2} + \frac{Q_\varepsilon{}^2}{j\omega c_s\left(1 + Q_\varepsilon{}^2\right)} \qquad 4.2$$

where Q_ε represents the quality factor of the BST dielectric layer and is reciprocally equal to the dielectric loss. Therefore, the real part of the measured impedance tends to R_{ser} at higher frequencies, in this case $R_{ser} \approx 0.55\ \Omega$.

To find out the sheet resistance R_s of the SMO bottom electrode and the dielectric constant of the BST film ε_r, the impedance of two test structures with similar outer but different inner diameters are subtracted, following Eq. 4.3.

$$Z_1 - Z_2 = \frac{R_s}{2\pi}\ln\frac{D_2}{D_1} + \frac{1}{j\omega\pi\varepsilon_r\varepsilon_0}\left(\frac{1}{{D_1}^2} - \frac{1}{{D_2}^2}\right) \quad 4.3$$

Such a subtraction eliminates the influence of the outer ring area [44], provided that similar values of L_s and R_p in the two test structures be assumed. This calculation for the two test structures with D_{out}= 400 µm and inner diameters of D_1 = 20 and D_2 = 40 µm gives R_s = 1.85 Ω/□ as the sheet resistance of the SMO, translating into 50 µΩ.cm of resistivity, which is in good agreement with the electrical characterisation on the SMO films using CPW structures [7]. Furthermore, the permittivity of the BST dielectric layer is calculated to be ε_r = 180. This value is equal to the calculated ε_r using the simple formula of $C = \varepsilon_0\varepsilon_r A/d$ using the measured capacitance C, the area of the signal pad A, and the thickness of the dielectric layer d. These results confirm that the contribution of the ground capacitance can be neglected.

The measured quality factor of the test structure follows:

$$Q_{tot}^{-1} = \frac{1}{Q_e} + \frac{1}{Q_\varepsilon} = \tan\delta_{tot} \quad 4.4$$

where the quality factor of the dielectric BST is proportional to the frequency, C_s and R_{BST}.

$$Q_\varepsilon = \frac{1}{\tan\delta_\varepsilon} = \omega C_s R_{BST} \quad 4.5$$

and

$$Q_{SMO} = \frac{1}{\tan\delta_{SMO}} = \frac{{Q_\varepsilon}^2}{\omega R_{SMO}\, c_p\left(1 + {Q_\varepsilon}^2\right)} \quad 4.6$$

To separate the Q_ε and Q_{SMO}, the measured insertion loss curves were fitted by the MoM RF solver and the ADS equivalent circuit modeling tool (Fig. 4.15). To have a good agreement between the measured, modeled, and simulated reflection coefficient curves in the whole

frequency range of 100 MHz to 10 GHz, the dielectric loss tangent was set in both methods to 0.008 (at 10 GHz).

A BST loss of 0.008 translates into a quality factor of 125 for BST at 10 GHz. The total quality factor of the test structure at lower frequencies (i.e. 1MHz) should equal this value. By extrapolation of the blue curve in the Fig 4.12, similar values for the total quality factor of the structure are achieved. In the outlooks of this work, characterization of the quality factor of the device at KHz-MHz frequencies is planned.

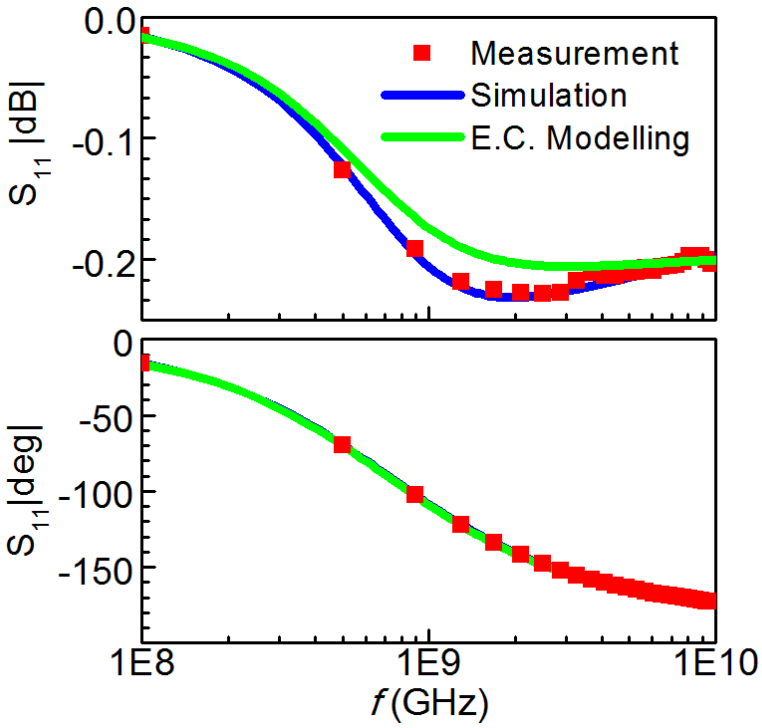

Fig. 4.15 Fitting of the measured reflection coefficient (red dots) in the unbiased state (0V) with the equivalent circuit model (green) and the MoM simulation (blue).

Using equation 4.6, the contribution of the conductor layer (SMO) and the dielectric layer (BST) to the total Q of the test structure can be separated. Fig 4.16 shows the results of fitting the measurement and simulation for the quality factor of the whole test structure, the conductor, and the dielectric layer.

As it can be seen in Fig. 4.16, the slope of the total varactor Q follows that of the BST at the low frequencies (f < ~300MHz). For frequencies above ~300 MHz, the total quality factor is dominated by the sharply dropping SMO quality factor. This results in the quick decay of the device quality factor at higher frequencies, especially in the GHz frequency range. The BST loss tangent of around 0.008 up to 10 GHz is among the lowest reported values of dielectric

loss. Fig. 4.16 shows the frequency dependence of the extracted BST loss tangent in this work in comparison to the best of the reported values in the literature for the most common electrode materials used so far.

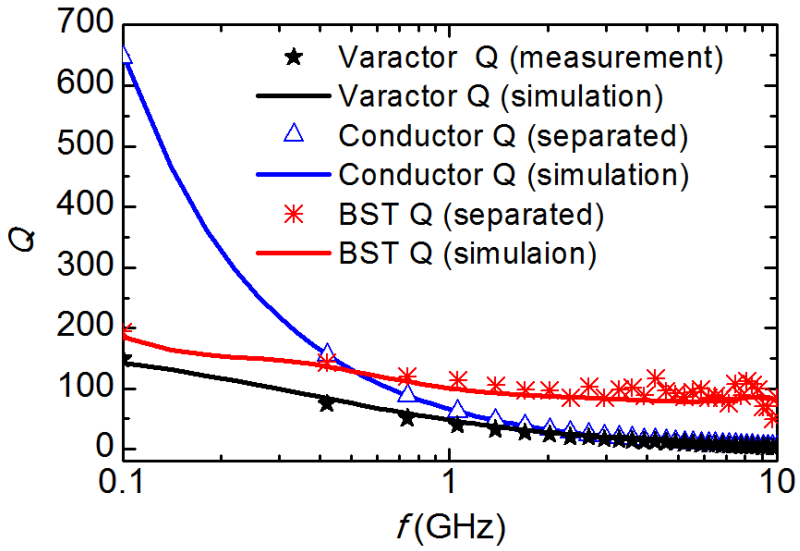

Fig. 4.16 Total (measured) quality factor of the MIM varactor (black), the extracted SMO quality factor (blue), and the extracted BST quality factor (red).

The dashed lines are the reproduction of the data from the literature. The corresponding sources are listed in the figure caption. As it can be seen, the loss tangent of the dielectric BST layer in this work is around 0.008 for frequencies up to 10 GHz. this value is lower than most of the values reported so far. Further optimization of the BST layer, for example by defect engineering, can further minimize the loss tangent in the future.

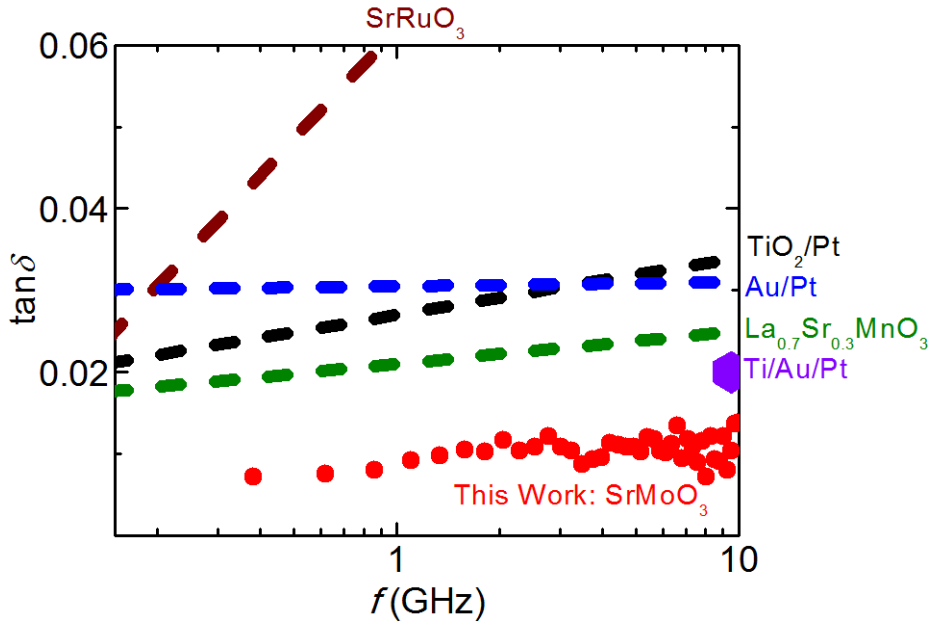

Fig. 4.17. Extracted loss tangent of the BST dielectric layer versus Frequency for the reported varactors using various bottom electrodes: $SrRuO_3$ [21], Au/Pt [43], $La_{0.7}Sr_{0.3}MnO_3$ [82], Ti/Au/Pt [83], TiO_2/Pt [83].

5. Summary

This work presents the revival of the concept of all-oxide thin-film ferroelectric varactors. A series of systematic approaches has yielded to intermediate success stories and eventually to the fabrication and characterization of a state-of-the-art oxide thin-film ferroelectric varactor. By utilizing the $SrMoO_3$ thin film as a conducting oxide, the $Ba_{0.4}Sr_{0.6}TiO_3$ thin film as an excellent dielectric material, and $SrTiO_3$ thin film as oxygen diffusion barrier between the conductor and the dielectric layer, it is shown that all-oxide varactors with excellent crystal quality and promising electrical properties at microwave frequencies can be achieved.

Epitaxial growth of $SrMoO_3$, $Ba_{0.4}Sr_{0.6}TiO_3$, and $SrTiO_3$ on 5×5 mm^2 (110) $GdScO_3$ single crystal substrate using Pulsed laser deposition (PLD) was achieved. Furthermore, deposition conditions were fine-tuned for epitaxial growth of fully commensurate thin-film stack of $SrTiO_3/SrMoO_3/SrTiO_3/Ba_{0.4}Sr_{0.6}TiO_3$ on $GdScO_3$ substrate. A KrF excimer laser with a wavelength of 248nm, fluence of 0.5 – 1 J/cm^2, and pulse rate of 2-5 Hz was used in the PLD system. The $SrTiO_3/SrMoO_3/SrTiO_3$ tri-layer was grown at ultra-high vacuum ($P<1\cdot10E\text{-}8$) with a substrate temperature of $T_{sub}=650$ C. The $Ba_{0.4}Sr_{0.6}TiO_3$ thin film was grown in oxygen pressure of 1 mTorr and a substrate temperature of $T_{sub}=630$ C. The growth of all the layers was monitored by an *in situ* RHEED system, suggesting a layer by layer growth for the entire heteroepitaxial stack. In order to realize top contacts and characterize the electrical properties of the test structure, an *ex situ* photolithographic lift-off process was optimized to coat a photoresist mask on the sample followed by magnetron sputtering of platinum and gold thin films. Top electrode patterns with central circular pad as the signal contact and concentric ring as ground contact were realized. Size of the top contact pads were varied to retrieve various material related properties from the measured data.

X-ray diffraction (XRD) *θ-2θ* scans and reciprocal space maps were used to monitor the single-phase growth of the heteroepitaxial stack, commensurate to the substrate, following epitaxial relation of $Ba_{0.4}Sr_{0.6}TiO_3$ [001] || $SrMoO_3$ [001] || $GdScO_3$ [110] and $Ba_{0.4}Sr_{0.6}TiO_3$ [100] || $SrMoO_3$ [100] || $GdScO_3$ [001]. Symmetric Laue oscillations in the vicinity of 002 $SrMoO_3$ and $Ba_{0.4}Sr_{0.6}TiO_3$ reflections suggest a homogeneous growth of both layers. For the same reflections, rocking curves with low diffusive background and full width at half maxima (FWHM) of below 0.05° suggest low defect densities in both thin films. Moreover, a Scanning Transmission Electron Microscopy (STEM) of the cross-section of the sample reconfirmed the commensurate relation of the heterostructure and atomically sharp interface between all the layers.

Excellent electrical properties of all-oxide varactors were achieved. A relative permittivity of 180 at room-temperature with 50% tunability at 8V is a reasonably high tunability, specially at such a low voltage. This opens the door to the possibility of tuning varactors with lower voltages, which is an attractive option for mobile devices. The quality factor of the test structure was measured between 10 MHz to 20 GHz. A quality factor of 180 under 8V of bias at 30 MHz suggests a very low dielectric loss of the BST dielectric layer. At frequencies above 400 MHz the quality factor decreased due to the losses in the $SrMoO_3$ layer. A commutation quality factor (CQF) of 10^4, 10^2, 10 at 100 MHz, 1 GHz, and 10 GHz, respectively, was achieved. Even at high frequencies, the value of CQF was more than 50 times higher than previously-reported values for BST varactors with $SrRuO_3$ conductor layer.

A wet chemical etching approach for selective etching of the meta-stable SMO thin films was offered. This study suggests that the etching rate of $SrMoO_4$ is much higher than that of the $SrMoO_3$. Thus, it is possible to use oxidizing additives such as H_2O_2 in alkaline solutions to modify the etching rate of the SMO. Furthermore, it was shown that by using low concentrations of alkaline solutions the removal of the superficial $SrMoO_4$ from the $SrMoO_3$ surface is easily possible. This method opens the possibility of dissolving the unwanted superficial $SrMoO_4$ for ex-situ characterization and measurement purposes, as well as device fabrication. In conclusion, a controllable and reliable method for wet chemical etching of the SMO was established. The knowledge acquired from this work can be used to pattern SMO thin films in the future in the fabrication of microelectronic devices. The etching approach offers a simple, economic, and scalable method to process the SMO for prospective industrial integration.

6. Outlook

In this work, the potential of $SrMoO_3$ as an excellent material for integration as a bottom electrode in the thin-film all-oxide ferroelectric varactors has been exhibited and a processing and characterization routine has been established to optimize the material properties and engineer a prototype thin-film all-oxide ferroelectric varactor.

In order to establish an industrial approach for fabrication of all oxide thin-film varactors it is necessary to prove the feasibility and viability of such a process through a prototype varactor. An interdisciplinary VIP+ project from the Federal Ministry of Education and Research in Germany (BMBF) is inspired from this work. The goal is to achieve a better performance by material and design optimization of the all-oxide ferroelectric thin-film varactors and to fabricate a prototype of state-of-the-art all oxide varactor using $SrMoO_3$ as the bottom electrode, aiming at better performance as compared to commercially available varactors. Continuation of this research work will encompass:

1. Substitution of $GdScO_3$ with cheaper substrates such as silicon or MgO which are more applicable in industrial fabrication set-ups.
2. Lowering the resistance of the conductor layer by achieving lower resistivity of SMO thin film or depositing thicker single crystalline $SrMoO_3$ layer.
3. Migration to more conventional deposition methods with the goal of lowering the fabrication costs and facilitating the industrial integration.
4. Engineering the $SrMoO_3$/$SrTiO_3$/BST interface in order to be able to keep the meta-stable $SrMoO_3$ intact while using higher oxygen pressures for deposition of the BST and thus lowering the density of oxygen vacancies in the BST layer for better material performance. In this context, it might be possible to substitute the $SrTiO_3$ capping layer with a different capping material which has a higher oxygen diffusion barrier, to allow higher oxygen pressure during the BST growth and thus decrease the oxygen vacancy density in the BST layer.
5. Design and optimization of a prototype varactor will conclude the initial research work on this set of material and shed light on the enormous potential of thin-film $SrMoO_3$ for microwave applications.

7. BIBLIOGRAPHY

[1] N. Setter, D. Damjanovic, L. Eng, G. Fox, S. Gevorgian, S. Hong, a. Kingon, H. Kohlstedt, N. Y. Park, G. B. Stephenson, I. Stolitchnov, a. K. Taganstev, D. V. Taylor, T. Yamada, and S. Streiffer, "Ferroelectric thin films: Review of materials, properties, and applications," *J. Appl. Phys.*, vol. 100, no. 5, pp. 1–46, 2006.

[2] A. I. Kingon and S. K. Streiffer, "Ferroelectric films and devices," *Curr. Opin. Solid State Mater. Sci.*, vol. 4, no. 1, pp. 39–44, 1999.

[3] G. Subramanyam, M. W. Cole, N. X. Sun, T. S. Kalkur, N. M. Sbrockey, G. S. Tompa, X. Guo, C. Chen, S. P. Alpay, G. A. Rossetti, K. Dayal, L.-Q. Chen, and D. G. Schlom, "Challenges and opportunities for multi-functional oxide thin films for voltage tunable radio frequency/microwave components," *J. Appl. Phys.*, vol. 114, no. 19, p. 191301, 2013.

[4] H. Y. Hwang, Y. Iwasa, M. Kawasaki, B. Keimer, N. Nagaosa, and Y. Tokura, "Emergent phenomena at oxide interfaces," *Nat. Publ. Gr.*, vol. 11, no. 2, pp. 103–113, 2012.

[5] C. Lee, N. D. Orloff, T. Birol, Y. Zhu, V. Goian, E. Rocas, R. Haislmaier, E. Vlahos, J. A. Mundy, L. F. Kourkoutis, Y. Nie, M. D. Biegalski, J. Zhang, M. Bernhagen, N. A. Benedek, Y. Kim, J. D. Brock, R. Uecker, X. X. Xi, V. Gopalan, D. Nuzhnyy, S. Kamba, D. A. Muller, I. Takeuchi, J. C. Booth, C. J. Fennie, and D. G. Schlom, "Exploiting dimensionality and defectmitigation to create tunable microwave dielectrics" Nat. Lett., vol. 502, p.532–536

[6] A. Radetinac, K. S. Takahashi, L. Alff, M. Kawasaki, and Y. Tokura, "Single-crystalline $CaMoO_3$ and $SrMoO_3$ films grown by pulsed laser deposition in a reductive atmosphere," *Appl. Phys. Express*, vol. 3, no. 7, 2010.

[7] A. Radetinac, A. Mani, S. Melnyk, M. Nikfalazar, J. Ziegler, Y. Zheng, L. Alff, P. Komissinskiy, A. Radetinac, A. Mani, S. Melnyk, and M. Nikfalazar, "Highly conducting $SrMoO_3$ thin films for microwave applications," *Appl. Phys. Lett.*, vol. 105, p. 114108, 2014.

[8] J. H. Haeni, P. Irvin, W. Chang, R. Uecker, P. Reiche, Y. L. Li, S. Choudhury, W. Tian, M. E. Hawley, B. Craigo, a K. Tagantsev, X. Q. Pan, S. K. Streiffer, L. Q. Chen, S. W. Kirchoefer, J. Levy, and D. G. Schlom, "Room-temperature ferroelectricity in strained SrTiO3.," *Nature*, vol. 430, no. August, pp. 758–761, 2004.

[9] A. Vorobiev, P. Rundqvist, K. Khamchane, and S. Gevorgian, "Microwave loss mechanisms in $Ba_{0.25}Sr_{0.75}TiO_3$ thin film varactors," *J. Appl. Phys.*, vol. 96, no. 8, p. 4642, 2004.

[10] A. K. Tagantsev, V. O. Sherman, K. F. Astafiev, J. Venkatesh, and N. Setter, "Ferroelectric Materials for Microwave Tunable Applications," pp. 5–66, 2004.

[11] P. Bao, T. J. Jackson, X. Wang, and M. J. Lancaster, "Barium strontium titanate thin film varactors for room-temperature microwave device applications," *J. Phys. D. Appl. Phys.*, vol. 41, no. 6, p. 63001, 2008.

[12] a K. Tagantsev, V. O. Sherman, K. F. Astafiev, J. Venkatesh, and N. Setter, "Ferroelectric materials for microwave tunable applications," *J. Electroceramics*, vol. 11, no. 1–2, pp. 5–66, 2003.

[13] A. Ahmed, I. A. Goldthorpe, and A. K. Khandani, "Electrically tunable materials for microwave applications," *Appl. Phys. Rev.*, vol. 2, no. 1, p. 11302, 2015.

[14] J. B. L. Rao, D. P. Patel, and V. Krichevsky, "Voltage-controlled ferroelectric lens phased arrays," *IEEE Trans. Antennas Propag.*, vol. 47, no. 3, pp. 458–468, 1999.

[15] M. J. Lancaster, J. Powell, and a Porch, "Thin-film ferroelectric microwave devices," *Supercond. Sci. Technol.*, vol. 11, pp. 1323–1334, 1999.

[16] O. G. Vendik, E. K. Hollmann, A. B. Kozyrev, and A. M. Prudan, "Ferroelectric Tuning of Planar and Bulk Microwave Devices," *J. Supercond.*, vol. 12, no. 2, pp. 325–338, 1999.

[17] F. A. Miranda, F. W. Van Keuls, R. R. Romanofsky, C. H. Mueller, S. Alterovitz, and G. Subramanyam, "Ferroelectric Thin Films-Based Technology for Frequency- and

Phase-Agile Microwave Communication Applications," *Integr. Ferroelectr.*, vol. 42, no. 1, pp. 131–149, 2002.
[18] R. Jakoby, P. Scheele, S. Muller, and C. Weil, "Nonlinear dielectrics for tunable microwave components," in *15th International Conference on Microwaves, Radar and Wireless Communications (IEEE Cat. No.04EX824)*, 2004, vol. 2, pp. 369–378.
[19] M. P. J. Tiggelman, K. Reimann, J. Liu, M. Klee, W. Keur, R. Mauczock, J. Schmitz, and R. J. E. Hueting, "Identifying dielectric and resistive electrode losses in high-density capacitors at radio frequencies," *IEEE Int. Conf. Microelectron. Test Struct.*, pp. 190–195, 2008.
[20] O. G. Vendik, L. T. Ter-Martirosyan, and S. P. Zubko, "Microwave losses in incipient ferroelectrics as functions of the temperature and the biasing field," *J. Appl. Phys.*, vol. 84, no. 2, p. 993, 1998.
[21] K. Khamchane, A. Vorobiev, T. Claeson, and S. Gevorgian, "$Ba_{0.25}Sr_{0.75}TiO_3$ thin-film varactors on $SrRuO_3$ bottom electrode," *J. Appl. Phys.*, vol. 99, no. 3, p. 34103, 2006.
[22] L. J. Sinnamon, R. M. Bowman, and J. M. Gregg, "Thickness-induced stabilization of ferroelectricity in $SrRuO_3/Ba_{0.5}Sr_{0.5}TiO_3$/Au thin film capacitors," *Appl. Phys. Lett.*, vol. 81, no. 5, p. 889, 2002.
[23] a. Lookman, J. McAneney, R. M. Bowman, J. M. Gregg, J. Kut, S. Rios, a. Ruediger, M. Dawber, and J. F. Scott, "Effects of poling, and implications for metastable phase behavior in barium strontium titanate thin film capacitors," *Appl. Phys. Lett.*, vol. 85, no. 21, p. 5010, 2004.
[24] J. B. Wachtman and R. a Haber, "CERAMIC FILMS AND COATINGS", *North publications*, 1993.
[25] J. F. Scott, "Ferroelectric memories," *Phys. World*, vol. 8, no. 2, pp. 46–50, 1995.
[26] B. Jamali, "The Evolution of RFID," in *Handbook of Smart Antennas for RFID Systems*, 2010, pp. 1–12.
[27] Y. H. Chun, J. S. Hong, P. Bao, T. J. Jackson, and M. J. Lancaster, "BST-varactor tunable dual-mode filter using variable ZC transmission line," *IEEE Microw. Wirel. Components Lett.*, vol. 18, no. 3, pp. 167–169, 2008.
[28] K. B. Kim, T. S. Yun, J. C. Lee, M. Chaker, C. S. Park, and K. Wu, "Integration of microwave phase shifter with BST varactor onto TiO_2/Si wafer.," *Electron. Lett.*, vol. 43, no. 14, pp. 757–759, 2007.
[29] K. B. Kim and C. S. Park, "Application of RF varactor using $Ba_xSr_{1-x}TiO_3/TiO_2$/HR-Si substrate for reconfigurable radio," *IEEE Trans. Ultrason. Ferroelectr. Freq. Control*, vol. 54, no. 11, pp. 2227–2232, 2007.
[30] A. Jamil, T. S. Kalkur, and N. Cramer, "Tunable ferroelectric capacitor-based voltage-controlled oscillator," *IEEE Trans. Ultrason. Ferroelectr. Freq. Control*, vol. 54, no. 2, pp. 222–226, 2007.
[31] D. S. Korn and H.-D. Wu, "A comprehensive review of microwave system requirements on thin-film ferroelectrics," *Integr. Ferroelectr.*, vol. 24, no. 1–4, pp. 215–237, 1999.
[32] H. Jiang, M. Patterson, D. Brown, C. Zhang, K. Pan, G. Subramanyam, D. Kuhl, K. Leedy, and C. Cerny, "Miniaturized and reconfigurable CPW square-ring slot antenna loaded with ferroelectric BST thin film varactors," *IEEE Trans. Antennas Propag.*, vol. 60, no. 7, pp. 3111–3119, 2012.
[33] R. A. York, "Tunable Dielectrics for RF Circuits," *Multifunct. Adapt. Microw. Circuits Syst.*, pp. 1–54, 2009.
[34] York R. *et al*, "Microwave integrated circuits using thin-film BST," in *IEEE International Symposium on Applications of Ferroelectrics*, 2000, vol. 1, pp. 195–200.
[35] M. P. J. Tiggelman, K. Reimann, F. Van Rijs, J. Schmitz, and R. J. E. Hueting, "On the trade-off between quality factor and tuning ratio in tunable high-frequency capacitors," *IEEE Trans. Electron Devices*, vol. 56, no. 9, pp. 2128–2136, 2009.
[36] S. V Razumov, A. V Tumarkin, M. M. Gaidukov, A. G. Gagarin, A. B. Kozyrev, O. G. Vendik, A. V Ivanov, O. U. Buslov, V. N. Keys, L. C. Sengupta, and X. Zhang, "Characterization of quality of $Ba_xSr_{1-x}TiO_3$ thin film by the commutation quality factor

measured at microwaves," *Appl. Phys. Lett.*, vol. 81, no. 9, pp. 1675–1677, 2002.
[37] P. Rundqvist, a. Vorobiev, E. Kollberg, and S. Gevorgian, "Large signal circuit model of parallel-plate ferroelectric varactors," *J. Appl. Phys.*, vol. 100, no. 2006, pp. 1–9, 2006.
[38] M. Tyunina and J. Levoska, "The paraelectric state in thin-film (Ba,Sr)TiO_3," *J. Appl. Phys.*, vol. 101, no. 8, pp. 0–7, 2007.
[39] S. Gevorgian, a. Vorobiev, and T. Lewin, "dc field and temperature dependent acoustic resonances in parallel-plate capacitors based on $SrTiO_3$ and $Ba_{0.25}Sr_{0.75}TiO_3$ films: Experiment and modeling," *J. Appl. Phys.*, vol. 99, no. 12, p. 124112, 2006.
[40] H. T. Lue and T. Y. Tseng, "Application of on-wafer TRL calibration on the measurement of microwave properties of $Ba_{0.5}Sr_{0.5}TiO_3$ thin films," *IEEE Trans. Ultrason. Ferroelectr. Freq. Control*, vol. 48, no. 6, pp. 1640–1647, 2001.
[41] J. H. Park, C. W. Baek, Sanghwa-Jung, H. T. Kim, Y. Kwon, and Y. K. Kim, "Novel micromachined CPW transmission lines for application in millimeter-wave circuits," in *Digest of Papers - International Microprocesses and Nanotechnology Conference, MNC 2000*, pp. 86–87.
[42] S. S. Gevorgian, "Basic characteristics of two layered substrate coplanar waveguides," *Electron. Lett.*, vol. 30, no. 15, pp. 1236–1237, 1994.
[43] R. De Paolis, F. Coccetti, F.- Pessac, and G. Guegan, "Microwave Characterization of Ferroelectric Thin Films for Novel Compact Tunable BST Filters," *Microwave Conference (EuMC), 2013 European,* pp. 8–11, 2013.
[44] Z. Ma, A. J. Backer, P. Polakos, H. Huggins, J. Pastalan, H. Wu, K. Watts, Y. H. Wong, and P. Mankiewich, "RF measurement technique for characterizing thin dielectric films," *IEEE Trans. Electron Devices*, vol. 45, no. 8, pp. 1811–1816, 1998.
[45] Y. Iwazaki, K. Ohta, and T. Suzuki, "Elimination of parasitic effects due to measurement conditions of SrTiO3 thin films up to 40 GHz," *J. Eur. Ceram. Soc.*, vol. 26, pp. 1841–1844, 2006.
[46] N. Delmonte, B. E. Watts, G. Chiorboli, P. Cova, and R. Menozzi, "Test structures for dielectric spectroscopy of thin films at microwave frequencies," *Microelectron. Reliab.*, vol. 47, pp. 682–685, 2007.
[47] S. C. Sejas-garc, "Complex Permittivity Determination of Thin-Films Through RF-Measurements of a MIM Capacitor," vol. 24, no. 11, pp. 805–807, 2014.
[48] W. Chen, K. G. McCarthy, A. Mathewson, M. Copuroglu, S. O'Brien, and R. Winfield, "Capacitance and *S*-Parameter Techniques for Dielectric Characterization With Application to High-*k* PMNT Thin-Film Layers," *IEEE Trans. Electron Devices*, vol. 59, no. 6, pp. 1723–1729, 2012.
[49] O. G. Vendik and S. P. Zubko, "Ferroelectric phase transition and maximum dielectric permittivity of displacement type ferroelectrics ($Ba_xSr_{1-x}TiO_3$)," *J. Appl. Phys.*, vol. 88, no. 9, pp. 5343–5350, 2000.
[50] Y. Gim, T. Hudson, Y. Fan, C. Kwon, A. T. Findikoglu, B. J. Gibbons, B. H. Park, and Q. X. Jia, "Microstructure and dielectric properties of $Ba_xSr_{1-x}TiO_3$ films grown on $LaAlO_3$ substrates," *Appl. Phys. Lett.*, vol. 77, no. 8, pp. 1200–1202, 2000.
[51] A. Sirenko, C. Bernhard, a Golnik, A. Clark, J. Hao, W. Si, and X. Xi, "Soft-mode hardening in $SrTiO_3$ thin films," *Nature*, vol. 404, no. 6776, pp. 373–6, 2000.
[52] A. Sirenko, I. Akimov, J. Fox, a. Clark, H.-C. Li, W. Si, and X. Xi, "Observation of the First-Order Raman Scattering in $SrTiO_3$ Thin Films," *Phys. Rev. Lett.*, vol. 82, no. 22, pp. 4500–4503, 1999.
[53] W. Chang, J. S. Horwitz, A. C. Carter, J. M. Pond, S. W. Kirchoefer, C. M. Gilmore, and D. B. Chrisey, "The effect of annealing on the microwave properties of $Ba_{0.5}Sr_{0.5}TiO_3$ thin films," *Appl. Phys. Lett.*, vol. 74, no. 7, p. 1033, 1999.
[54] K. Natori, D. Otani, and N. Sano, "Thickness dependence of the effective dielectric constant in a thin film capacitor," *Appl. Phys. Lett.*, vol. 73, no. 5, pp. 632–634, 1998.
[55] D. P. Norton, "Synthesis and properties of epitaxial electronic oxide thin-film materials," *Mater. Sci. Eng. R Reports*, vol. 43, no. 5–6, pp. 139–247, 2004.
[56] T. Ohnishi, H. Koinuma, and M. Lippmaa, "Pulsed laser deposition of oxide thin films,"

in *Applied Surface Science*, 2006, vol. 252, no. 7, pp. 2466–2471.
[57] Can Wang, B. L. Cheng, S. Y. Wang, H. B. Lu, Y. L. Zhou, Z. H. Chen, and G. Z. Yang, "Effects of oxygen pressure on lattice parameter, orientation, surface morphology and deposition rate of $Ba_{0.02}Sr_{0.98}TiO_3$ thin films grown on MgO substrate by pulsed laser deposition," *Thin Solid Films*, vol. 485, pp. 82–89, 2005.
[58] W. Braun, *Applied RHEED Reflection High-Energy Electron Diffraction During Crystal Growth*, vol. 154. 1999.
[59] A. J. Jacobson, "Materials for solid oxide fuel cells," *Chemistry of Materials*, vol. 22, no. 3. pp. 660–674, 2010.
[60] I. Kojima and B. Li, "Structural characterization of thin films by X-ray reflectivity," *Rigaku J.*, vol. 16, no. 2, pp. 31–42, 1999.
[61] K. Inaba, "X-ray thin-film measurement techniques I . Overview," *Rigaku J.*, vol. 24, no. 1, 2008.
[62] T. Mitsunaga, "X-ray thin-film measurement techniques II. Out-of-plane diffraction measurements," *Rigaku J.*, vol. 25, no. 1, pp. 7–12, 2009.
[63] T. Konya, "X-ray thin-film measurement techniques III. High resolution X-ray diffractometry," *Rigaku J.*, vol. 25, no. 2, p. 2009, 2009.
[64] P. S. Prevéy, "X-ray diffraction residual stress techniques," *Met. Handbook. 10. Met. Park*, no. 513, pp. 380–392, 1986.
[65] A. Pimpin and W. Srituravanich, "Reviews on micro- and nanolithography techniques and their applications," *Eng. J.*, vol. 16, no. 1, pp. 37–55, 2012.
[66] R. F. Pease and S. Y. Chou, "Lithography and other patterning techniques for future electronics," *Proc. IEEE*, vol. 96, no. 2, pp. 248–270, 2008.
[67] B. D. Gates, Q. Xu, M. Stewart, D. Ryan, C. G. Willson, and G. M. Whitesides, "New approaches to nanofabrication: Molding, printing, and other techniques," *Chemical Reviews*, vol. 105, no. 4. pp. 1171–1196, 2005.
[68] R. F. Pease, "Maskless lithography," *Microelectronic Engineering*, 2005, vol. 78–79, no. 1–4, pp. 381–392.
[69] J. Melngailis, "Focused ion beam technology and applications," *J. Vac. Sci. Technol. B Microelectron. Nanom. Struct.*, vol. 5, no. 2, p. 469, 1987.
[70] M. J. Madou, "Fundamentals of Microfabrication: The Science of Miniaturization," *Fundamentals of Microfabrication: The Science of Miniaturization*, 2002, p. 49.
[71] M. Altissimo, "E-beam lithography for micro-/nanofabrication," *Biomicrofluidics*, vol. 4, no. 2, 2010.
[72] C. Vieu, F. Carcenac, A. Pepin, Y. Chen, M. Mejias, A. Lebib, L. Manin-Ferlazzo, L. Couraud, and H. Launois, "Electron beam lithography: resolution limits and applications," *Appl. Surf. Sci.*, vol. 164, no. 1, pp. 111--117, 2000.
[73] R. D. Piner, "'Dip-Pen' Nanolithography," *Science*, vol. 283, no. 5402, pp. 661–663, 1999.
[74] L. L. López, J. Portelles, J. M. Siqueiros, G. A. Hirata, and J. McKittrick, "$Ba_{0.5}Sr_{0.5}TiO_3$ thin films deposited by PLD on SiO_2/Si RuO_2/Si and Pt/Si electrodes," *Thin Solid Films*, vol. 373, no. 1–2, pp. 49–52, 2000.
[75] M. D. Biegalski, J. H. Haeni, S. Trolier-McKinstry, D. G. Schlom, C. D. Brandle, and a. J. V. Graitis, "Thermal expansion of the new perovskite substrates $DyScO_3$ and $GdScO_3$," *J. Mater. Res.*, vol. 20, no. 4, pp. 952–958, 2005.
[76] T. R. Taylor, P. J. Hansen, B. Acikel, N. Pervez, R. A. York, S. K. Streiffer, and J. S. Speck, "Impact of thermal strain on the dielectric constant of sputtered barium strontium titanate thin films," *Appl. Phys. Lett.*, vol. 80, no. 11, pp. 1978–1980, 2002.
[77] J. Krupka, J. Breeze, A. Centeno, N. Alford, T. Claussen, and L. Jensen, "Measurements of permittivity, dielectric loss tangent, and resistivity of float-zone silicon at microwave frequencies," *IEEE Trans. Microw. Theory Tech.*, vol. 54, no. 11, pp. 3995–4000, 2006.
[78] Y. Kozuka, H. Seki, T. C. Fujita, S. Chakraverty, K. Yoshimatsu, H. Kumigashira, M. Oshima, M. S. Bahramy, R. Arita, and M. Kawasaki, "Epitaxially stabilized $EuMoO_3$: A new itinerant ferromagnet," *Chem. Mater.*, vol. 24, no. 19, pp. 3746–3750, 2012.

[79] I. Nagai, N. Shirakawa, S. I. Ikeda, R. Iwasaki, H. Nishimura, and M. Kosaka, “Highest conductivity oxide $SrMoO_3$ grown by a floating-zone method under ultralow oxygen partial pressure,” *Appl. Phys. Lett.*, vol. 87, no. 2, 2005.

[80] A. Radetinac, K. S. Takahashi, L. Alff, M. Kawasaki, and Y. Tokura, “Single-crystalline Sr_2MoO_4 films as prepared by pulsed laser deposition,” *J. Cryst. Growth*, vol. 322, no. 1, pp. 38–40, 2011.

[81] A. Vorobiev, P. Rundqvist, K. Khamchane, and S. Gevorgian, “Silicon substrate integrated high Q-factor parallel-plate ferroelectric varactors for microwave/ millimeterwave applications,” *Appl. Phys. Lett.*, vol. 83, no. 15, pp. 3144–3146, 2003.

[82] S. Sheng, X.-Y. Zhang, P. Wang, and C. K. Ong, “Effect of bottom electrodes on dielectric properties of high frequency $Ba_{0.5}Sr_{0.5}TiO_3$ parallel plate varactor,” *Thin Solid Films*, vol. 518, no. 10, pp. 2864–2866, 2010.

[83] C. V. Varanasi, K. D. Leedy, D. H. Tomich, and G. Subramanyam, “Large area $Ba_{1-x}Sr_xTiO_3$ thin films for microwave applications deposited by pulsed laser ablation,” *Thin Solid Films*, vol. 517, no. 9, pp. 2878–2881, 2009.